Advanced Sensor Research

ADVANCED SENSOR RESEARCH Open Access

www.advsensorres.com

RESEARCH ARTICLE OPEN ACCESS

A New Concept for an Integrated Mapping of Rare-Earth Elements using Laser–Induced Fluorescence and Reflectance Spectroscopy

Titus Abend[1] | Margret Fuchs[2] | Jan Beyer[1] | Sandra Lorenz[2] | Nadine Schüler[3] | Kay Dornich[3] | Johannes Heitmann[1,4] | Richard Gloaguen[2]

[1]Institute of Applied Physics, TU Bergakademie Freiberg, Freiberg, Germany | [2]Helmholtz-Zentrum Dresden-Rossendorf, Helmholtz Institute Freiberg for Resource Technology, Division of Exploration Technology, Freiberg, Germany | [3]Freiberg Instruments GmbH, Freiberg, Germany | [4]Department of Energy Materials and Test Devices, Fraunhofer, Institute of Integrated Systems and Device Technology, Erlangen, Germany

Correspondence: Margret Fuchs (m.fuchs@hzdr.de)

Received: 11 July 2025 | **Revised:** 13 February 2026 | **Accepted:** 25 February 2026

Keywords: laser-induced fluorescence (LIF) | line scan | photoluminescence (PL) | rare-earth elements (REE) | reflectance spectroscopy (HSI) | rocks | spectroscopy-based sensors

ABSTRACT

Rare earth elements are increasingly seen as critical raw materials and are currently the subject of geopolitical interests. To boost mineral exploration and extraction, it is important to ensure the rapid identification and mapping of rare earth elements, and non-invasive spectroscopy-based technologies could offer suitable solutions. We therefore investigated the potential of an integrated sensor system that combines hyperspectral and laser-induced fluorescence imaging as a non-invasive alternative characterization technique to conventional time-consuming and costly chemical analysis. To test the analytical procedure we used representative material from the Siilinjärvi mine (Finland) and from Lofdal (Namibia). Laser-induced fluorescence mapping results document the successful identification and efficient mapping of several rare earth elements within complex mineral matrices. The variation in laser-induced fluorescence excitation wavelength facilitates the selective mapping of specific rare earth elements, thereby enhancing their differentiation capabilities. The combination with hyperspectral imaging provides mineral maps and cross-validation. The major benefit of the integrated optical sensor system lies in the rapid acquisition of spatially continuous information on the occurrence and type of rare earth elements without the need for sample preparation. The non-destructive character and operation in line-scan mode opens manifold possibilities for in-line applications with continuous sample throughput.

1 | Introduction

The specific optical, chemical, and physical properties of rare earth elements (REEs) guarantee the functionality of many high-tech applications (e.g., hard-disk drives, displays, lasers, strong permanent magnets). Rare Earth Elements are in high demand due to their crucial role in green energy technologies, electronics, defense, industrial applications, and geopolitical factors. For example, Rare Earth Elements (REEs) are crucial in the production of high-performance magnets utilized in wind turbines and electric vehicle (EV) motors. With the global push toward carbon neutrality, the demand for REEs in renewable energy technologies has experienced a significant surge [1–3]. Concomitantly, the increasing technology-driven REE demand faces significant supply risks due to the globally strongly concentrated deposit exploitation, as well as economic challenges due to depleting or low grades deposits [4, 5]. The EU Commission included REEs in the list of Critical Raw Materials [6] in 2014.

https://doi.org/10.1002/adsr.202500103

REEs are naturally occurring minerals that are primarily found in carbonatites and alkaline igneous complexes. These complexes serve as the world's primary sources of REEs. The most significant REE-bearing minerals include bastnäsite, monazite, xenotime, apatite, and eudialyte, along with less common minerals such as parisite, synchysite, and allanite. These minerals are often associated with pegmatites, granites, metamorphic rocks, and placer deposits, which are formed through the erosion and concentration of REE-rich minerals in river or beach sands. Furthermore, REEs can be found in phosphorites, clay deposits, and ion-adsorption clays, particularly in southern China, where they are extracted through leaching processes.

Innovative, efficient technologies for REE exploration and process monitoring are crucial in order to ensure the discovery and economic exploitation of REE deposits. Modern bulk analysis gathers geochemical information in order to characterize the type and grade of REE deposits based on selected locations (e.g., core section samples). Currently, techniques like Inductively Coupled Plasma Mass Spectrometry (ICP-MS) provide highly accurate identification and quantification of individual REEs in rock samples. These techniques require destructive sampling and laboratory environments. Appropriate sample selection and analysis largely relies on manual work and comprehensive expert knowledge. These analysis methods are typically off-line, destructive methods and both time consuming and costly, especially when employed in routine applications. Laser-Induced Breakdown Spectroscopy (LIBS) can be used in-line and without sample preparation but provide point measurements and accurate concentration estimations depend on mineral phases. LIBS is routinely used in operational environment but is limited by the relatively small measurement surface (<<1mm) and poor single REE identification. LIBS is therefore more adapted to first order grade control in operational settings.

In addition to these techniques, reflectance spectroscopy has shown fundamental potentials for mineral mapping of rock surfaces from satellite scale down to lab-based sample scans. This non-destructive and imaging technology provides several advantages for in-line, fast and cost-efficient solutions dedicated to material characterization and identification. Reflectance spectroscopy and hyperspectral imaging exploit the absorption of electromagnetic radiation at certain energies, corresponding to specific excitations (these may be electronic or vibronic in nature) of a given material as the diagnostic basis for mineral identification [7–10].

The detection of specific REEs is thus performed by analyzing their unique absorption features in the visible-near infrared (VNIR) and shortwave infrared (SWIR) spectra. Most REEs (e.g., neodymium, cerium, dysprosium) possess distinct spectral signatures and a comprehensive overview of REE-related features acquired at lab-scale can be found in e.g., [11–13]. The first approaches to map REEs with remote sensing techniques integrated information from multiple scales to narrow down local REE distributions and improve robustness of detection results, e.g., [14, 15]. It proved very difficult to map REEs from large distance because of spatial and spectral resolutions of hyperspectral cameras. At ground spatial sampling >1m spectral information is composed by highly mixed mineral compositions and therefore the spectral signatures most REEs other than Nd are suppressed. Only the pronounced absorption features of Nd detected in the visible to near-infrared (VIS-NIR) range of the electromagnetic spectrum can serve as a key indicator for the presence of other REE, esp. of light REE (LREE) that occur collectively due to their similar chemical properties, see e.g., [14–17]. Boesche et al. [16] were able to infer bulk REE abundances in a rock outcrop based on Nd as a pathfinder element.

Remote sensing approaches also mainly rely on Nd-related absorptions in order to infer REE abundances. Booysen et al. [18] presented a robust Nd-based REE mapping of local extends using uncrewed aerial vehicles (UAVs) hyperspectral imaging (HSI) mapping at a carbonatite complex in Namibia and in Finland. Neave et al. [17] reviewed the performances of different satellites and suggested that some REEs could be detected from space under certain conditions. Following the same principle, EnMAP hyperspectral satellite data was used to map Nd in Mountain Pass, California. A polynomial fitting technique successfully mapped Nd's surface occurrence at a 30-meter pixel resolution [19].

Laser-induced fluorescence spectroscopy (LIF) provides a complementary method for non-invasive, optical spectroscopy-based REE identification [13, 20–24]. The method is based on the specific fluorescence emissions of most REEs. Excited by monochromatic lasers of matching energy, the incompletely filled 4f-orbitals allow characteristic radiative relaxation processes. The emission wavelengths represent the energy release during relaxation from the excited states of a given REE, which is additionally modulated by the electronic and crystal-lattice configuration within the host mineral [20, 21, 25]. Resulting diagnostic LIF signals represent spectral fingerprints that can be utilized for REE mapping in exploration, mining and recycling applications. Most characteristic fluorescence peaks are located in the VIS-NIR range and the identification of most REEs is possible, with the exception of La, Gd, Tm, Lu [24]. The distinct and narrow emission lines, particularly in the oxidation state 3+, are well suited to distinguish specific REEs from typically broadband mineral emissions e.g., [13, 21, 23, 26–29]. REE emission patterns can vary in different mineral phases and thus in various minerals such as apatite [29–32], calcite [29, 31], fluorite [28, 33], phosphate [24], or zircon [34]. These findings emphasise that concurring effects in the observed spectra due to emission overlaps, energy transfer effects and the crystalline configuration of the host mineral can affect the performance of REE detection with LIF in natural rocks. It is also widely recognized that the emission of rare earth elements (REE) is highly sensitive to the energy of the incident laser light, primarily due to the unique electronic structure of the shielded 4f orbitals. The optimized excitation energies for the most intense emissions vary significantly among different REE, thereby complicating the application of laser-induced fluorescence (LIF) to minerals that typically contain multiple REEs. While most studies utilize ultraviolet (UV) lasers for high-energy excitation, the use of blue or green lasers is more appropriate for REEs such as praseodymium (Pr), samarium (Sm), or neodymium (Nd), respectively. [21, 24]. The selection a specific excitation wavelength provides therefore the opportunity of exciting only those REEs, which respond to the given excitation energy [13, 23]. Successful LIF implementation in industrial operations was pioneered by e.g., [35, 36] for quality control in bulk sorting, by e.g., [37] for horizon control directly during raw material excavation, and by e.g., [38] for drill cores. The solutions were tailored to specific settings and target classes such as apatite versus non-apatite. However, industrial applications have not yet embraced the potential of selective, multi-band excitation.

A better characterization of REEs can be performed in a laboratory using the long decay times of REE luminescence following pulsed excitation. REE decay times differ significantly from the short decay times of most host mineral fluorescence bands. Several studies using time-resolved laser-induced fluorescence (TR-LIF) illustrated the detailed and robust identification of REE within minerals and rocks in laboratory e.g., [25, 31, 33, 39]. Fluorescence life-time imaging microscopy (FLIM) and its related techniques image differences in fluorescence decay times across the investigated sample, and hence, is a powerful tool in the field of REE analysis [40, 41]. The specific decay times allow to distinguish materials in laboratory even when they show spectrally overlapping fluorescence bands. The typical operation mode of these time-resolved techniques is a point-detection measurement, either as single validation points in spectroscopic lab research or as point-by-point raster-scan imaging for surface mapping. Such measurements are time-consuming, especially when large sample areas need to be assessed. Their applicability for extensive, routine applications in industrial operations is therefore limited. The requirement for complex, high-speed pulsed and synced hardware-software equipment needed for time-solved signal recording further complicates the introduction of TR-LIF in operational environments in the mining sector.

An operational technique to constrain the spatial extent, variability and geochemical association of REE occurrences has yet to be developed to provide efficient mapping solutions for exploration, process monitoring or recycling. In this work, we address three innovation dimensions. (1) We propose a new setup for line-scan LIF mapping compatible with state-of-the-art high-sensitivity HSI detectors, (2) we combining 3 specifically designed LIF excitation units for selective REE excitation and (3) we integrate the setup with reflectance mapping. The overall scope is the efficient combination of information for potential application in industrial operations. The integration of emission and absorption spectroscopy forms the basis for robust, cross-validated REE identification combined with information on host minerals. The advantage of their integration lies in their ability of REE-detection using recordings of the same equipment in the visible (VIS) to near-infrared (NIR). The seamless integration using a single detector for both methods sets ground for data fusion due to technically determined consistent measurement conditions. The line-scan strategy delivers an efficient option and a balanced solution for very low intensity LIF signals and orders of magnitude more intense reflectance signals.

In order to investigate the performance of this integrated approach as a robust and efficient in-line, non-destructive sensing technology for the exploration, mining and recycling industry, we (1) test the REE identification and mapping using a hyperspectral LIF line-scan setup, (2) evaluate results in comparison to reflectance HSI using the same line-scan camera, (3) exploit the versatility of LIF mapping with three different excitation wavelengths and (4) validate LIF-HSI mapping results based on geochemical analysis and mineral liberation analysis (MLA).

2 | Results and Discussion

2.1 | Mineral Characterization

We use the results of scanning electron microscopy-based MLA (SEM-MLA) together with RGB images to characterise the mineralogical context and spatial distribution of potential host minerals in our samples. Figure 1 depicts the mapping results of the MLA-based mineral classification (B) for sample FI17-GU06, collected from an active mine area from the Siilinjärvi carbonatite complex in Finland. The depicted mineral composition represents the best matches between entries in the mineral reference library of the MLA software and measured signals. For clarity and comparability, we grouped identified minerals into five dominant types (see MLA legend). The obtained major mineral types are resolved at high spatial resolution (4 μm pixel size) and resemble the color nuances visible in the original RGB image (Figure 1A). Most abundant are calcite, dolomite, apatite, biotite, and hematite. The calcite forms the dominant matrix of the sample with inclusions of dolomite crystals of variable size from mm to nearly cm scale and randomly scattered across the entire sample. The apatite crystals reflect an overprint of a later stage of inclusions into the calcite-dolomite composition. Biotite and hematite occur as small, local mineralisations at the upper right and randomly dispersed, respectively. The result reflects the reported overall mineralogy of the Siilinjärvi carbonatite complex, while the carbonatite ratio of calcite to dolomite shifted to roughly 3:1 (calcite: ca. 60.0 %, dolomite: ca. 24.5 %, see Table 1).

It is noted in detailed MLA results that the majority of calcite was detected as a mix with Fe, which is also evident in the reddish calcite color seen in the RGB image. The accessory apatite content is about 10.6 %. The apatite is expected to represent the major host of REEs [42]. Although not spatially resolved in the SEM-MLA map, also indications of small occurrences of further REE-bearing minerals, esp. monazite-(Ce) and xenotime-(Y), have been observed.

A similar picture of a predominant carbonate-apatite matrix is evident in the second sample, NA-RB03 from Lofdal, Namibia, but with differing quantitative mineral abundances (see Figure 2 and Table 1). The MLA result map documents a predominant calcite matrix, where overprints of apatite mineralisations occur in folded lenses distributed in a diagonal pattern from the lower right to the upper left corner. Other minerals (Table 1) comprise fluorite, goethite, chlorite, and quartz. REE-bearing minerals were detected in very small concentrations, mainly as xenotime-(Y). However, the calcite occurs to a significant degree in form of a mix with goethite, and furthermore, goethite is distributed in form of small crystals. Hence, the MLA mapping of predominant calcite needs to be taken with caution, because likely calcite pixel in the MLA map contain a mix of calcite with goethite. This causes the MLA map to under-represent the occurrence of goethite and seems to over-represent the calcite abundance. Our MLA result details confirm an abundance of ca. 0.27 wt.% pure calcite, but a mix of calcite-goethite with more than 77 wt%. The high goethite contribution is supported by the strong reddish color of the sample (see RGB image in Figure 2A) dominating most calcite areas as well as by XRD results indicating that goethite contributes about 26 % to the sample's composition.

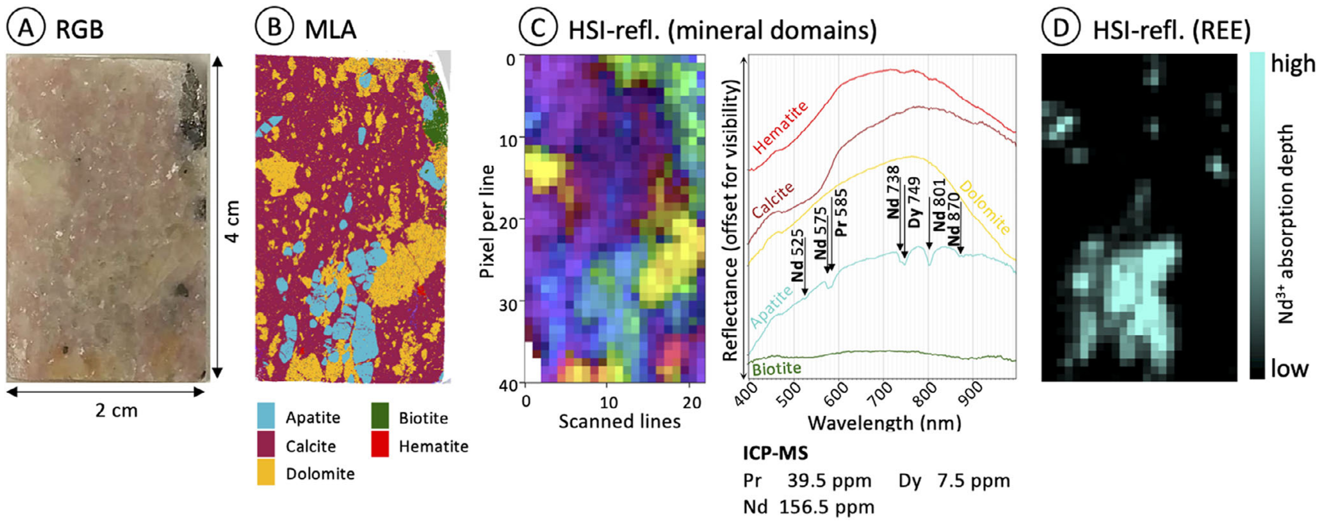

FIGURE 1 | Overview on MLA and reflectance HSI mapping results for FI17-GU06 from Siilinjärvi, Finland. (A) RGB image of the sample. (B) map of predominant minerals obtained by SEM-MLA. (C) saturation enhanced false color reflectance map (R-748 nm, G-550 nm and B-900 nm), and reflectance spectra of the main mineral domains including observed absorption feature position (in nm), associated REE and related ICP-MS results for comparison (for further details, see Table 4). (D) map of the normalized Nd^{3+} absorption depth at 801 nm obtained from reflectance HSI.

TABLE 1 | MLA and XRD results for mineral characterisation in %.

Sample ID	Method	Apatite	Calcite	Dolomite	Biotite	Hematite	
FI17-GU06	MLA	10.55	60.03	24.49	1.36	0.17	
Sample ID	**Method**	**Apatite**	**Calcite**	**Fluorite**	**Goethite**	**Chlorite**	**Quartz**
NA-RB03	MLA	9.37	82.76	1.38	1.25	0.97	1.80
	XRD	6.78	50.37	NA	25.92	NA	1.85

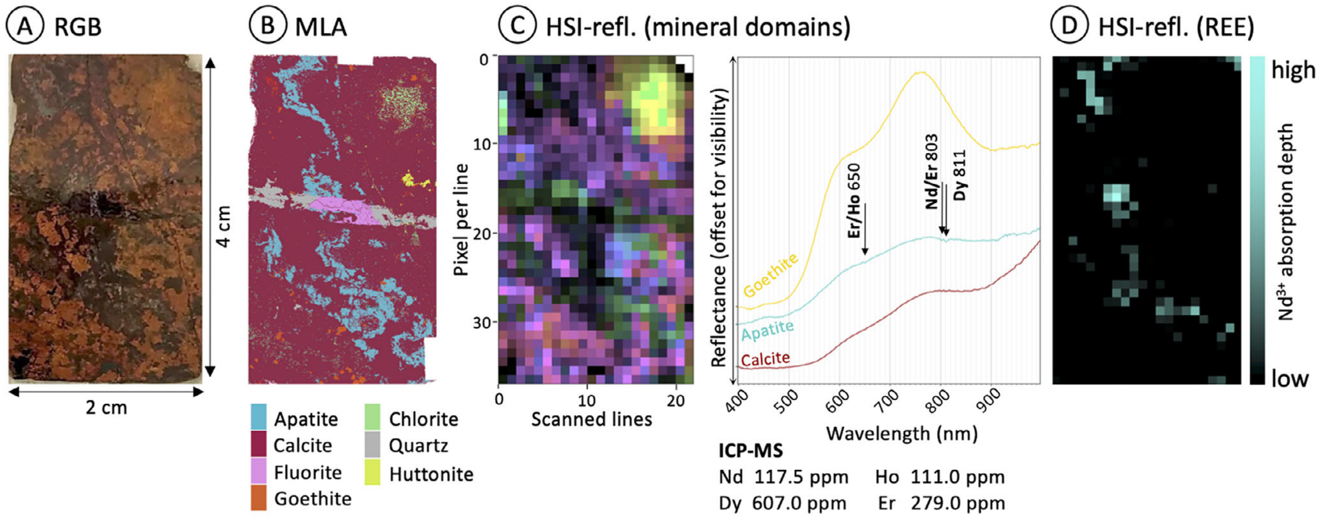

FIGURE 2 | Overview on MLA and reflectance HSI mapping results for NA-RB03 from Lofdal, Namibia. (A) RGB image of the sample. (B) map of predominant minerals obtained by SEM-MLA. (C) saturation enhanced false color reflectance map (R-748 nm, G-550 nm, and B-900 nm), and reflectance spectra of the main mineral domains including observed absorption feature position (in nm), associated REE and related ICP-MS results for comparison (for further details, see Table 4). (D) map of the normalized Nd^{3+} absorption depth at 580, 745, and 801 nm obtained from reflectance HSI.

2.2 | Reflectance Mapping Results

The acquired reflectance HSI data allowed the mapping of distinct mineral domains (Figures 1C and 2C) and REE containing areas (Figures 1D and 2D).

For sample FI17-GU06, the adopted band ratio approach is able to distinguish five mineral domains, which resemble the MLA-based mineral classes in type and overall distribution. The matrix is confirmed to be dominated by calcite. The reported occurrences of dolomite and apatite coincide with locations of large crystals, while smaller, dispersed mineral crystals (dolomite and hematite) of sizes below the detector's spatial resolution of 0.9 mm cannot be resolved and cause pixel with mixed spectra. This affects especially the mix of calcite and dolomite spectra, turning the pixel color code into purple shades.

Representative spectra of determined mineral domains show distinct patterns. Calcite is clearly marked by the broad absorption feature between 500 and 600 nm attributed to Fe ions and hence, confirms detailed information from MLA data (discussed above). The apatite spectra show a series of five REE-related absorption features at 525, 575, 738, 801, and 870 nm that can be mainly associated to Nd (Figure 1C right). However, two double features are evident, where the second position agrees to fingerprint positions of Pr (585 nm) and Dy (749 nm). The ICP-MS results for the detected REE, shown in Figure 1C right (cf. Table 4), confirm the dominance of LREE, detected as Nd and Pr. It is noted for this sample that also Dy is recognized, being representative of the heavy REE (HREE), although at a very low concentration. The other mineral domain spectra do not indicate any REE features and hence, we attribute REE occurrence to the apatite phase and interpret Nd to serve as REE pathfinder in this sample.

Mapping in turn the Nd^{3+}-related absorption depth detected at 801 nm (Figure 1D) confirms the observation from REE influenced apatite spectra by consistent spatial distribution of both, apatite and REE, while calcite and dolomite clearly disappear from the map (Figure 1D). The diagnostic fingerprint at 805 nm is a typical spectral absorption feature for neodymium caused by the corresponding electronic transition $^4I_{9/2} \rightarrow {}^4F_{3/2}$ of the trivalent neodymium ion [43]. The Nd^{3+} map of this 801 nm absorption depth can further highlight spatial intensity variations of the Nd feature. Highest depth values are achieved for the largest apatite crystals, while pixel of less pronounced depth indicate the reduction of feature significance with the degree of spectral mixing, because those pixel are located at mineral domain boundaries or where apatite crystals are smaller than the detector's spatial resolution.

For sample NA-RB03 (Figure 2), the mineral domain approach yielded three spectral classes corresponding to calcite, apatite, and goethite. Mapping the spatial distribution provides a quite in-homogeneous picture. Major differences to the MLA map are associated with the distribution of calcite. Here, the HSI reflectance map is able to distinguish Fe-containing calcite areas, seen as brown-reddish areas in the RGB image (Figure 2A, compared to B and C), as spectral domain from those calcite apparent as darkish-transparent areas with overall low reflectance response. The chosen MLA mapping and grouping approach fails to detail the observed differences in calcite mineralogy and related spectral signatures. The overall small crystal sizes of goethite and apatite within the calcite matrix results in mixed spectral information for many pixel seen in various color nuances, where apatite appears in bluish to greenish shades. Inspection of the mineral domain spectra (Figure 2C right) provides weak indication of REE features in apatite at two positions, 650 nm and and a double feature at 803 nm and 811 nm. The typical Nd-related series of absorption features is nearly vanished, only the weak absorption at 803 nm can be associated with Nd, but also Er might potentially contribute. The feature at 650 nm corresponds to fingerprint positions of Er and Ho, while the feature at 811 nm coincides with a Dy fingerprint. The overall spectral REE pattern clearly differs from the observations from the Siilinjärvi sample. The features are significantly weaker and identified REEs agree with ICP-MS results of higher contribution from HREE. Although the ICP-MS-based concentration of Nd is only a little less than in the Siilinjärvi sample, the concentrations of Dy, Ho, and Er is about 100 times higher, giving rise to the according interpretation of HREE being responsible for the observed weak spectral reflectance features.

The resulting HSI reflectance-based Nd-feature depth map aligns to the observations from the HSI reflectance-based mineral domains (Figure 2D). The spatial distribution mimics the apatite abundance observed in MLA result mapping and further enhances the visualization results from HSI reflectance. the latter suffered from spectral mixing and the spatial pixel resolution being coarser than most crystal sizes. Here, the mapping of Nd feature depth variations can better unravel the REE distribution associated with apatite, but as already stated, the spectral mixing together with weak features challenge the detection. However, comparable to the Siilinjärvi sample, the other mineral domains do not show an indication of REEs in their spectra (Figure 2C right) nor appear in the Nd feature mapping approach (Figure 2D) for this Lofdal sample.

2.3 | LIF Results for REE Mapping

Our integrated HSI setup for LIF line-scanning allowed to record distinct luminescence emission in both studied rock types, the Siilinjärvi sample FI17-GU06 from Finland and the Lofdal sample NA-RB03 from Namibia. The observed spectral patterns result from characteristic luminescence centers in the investigated material. We exemplify the applied pixel-wise classification of LIF mapping results using the sample FI17-GU06 from Siilinjärvi, Finland. Further details on recorded LIF data, their selective excitation results, and REE identification are given for both samples in the following section.

We identified four dominant LIF endmembers of distinct emission characteristics in sample FI17-GU06 using the SMACC-based endmember extraction. The LIF endmembers represent pure spectral components contributing in variable proportions to observed pixel spectra. The mixing of spectral information contained in individual pixels requires careful attention during classification, because pixel boundaries do not necessarily match with mineral boundaries. The degree of mixing in recorded spectra varies depending on the mineral crystal sizes, boundary

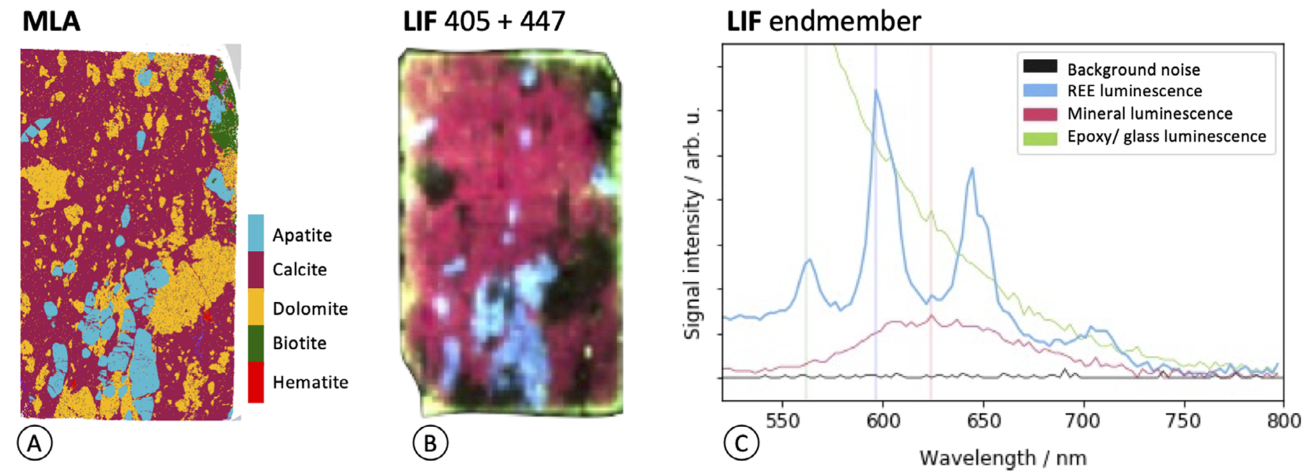

FIGURE 3 | Overview on MLA and LIF mapping results for FI17-GU06 from Siilinjärvi, Finland. (A) MLA mineral map of sample FI17-GU06. (B) Hyperspectral LIF map obtained under simultaneous excitation at 405 and 447 nm using a false-color representation based on the dominant spectral features of the identified endmembers (R-625 nm, G-562 nm, and B-597 nm). (C) LIF spectra of the results of the SMACC-based endmember extraction with four significant classes, the three vertical colored lines indicate the selected spectral positions of the RGB bands used in B.

positions, emission sensitivity, and spatial resolution of the detector. Similar to observations for HSI reflectance mapping, only the larger crystals of several mm in size are dominated by a single LIF endmember.

In order to address the mixing-related issues for classification, we used the extracted endmembers (see Experimental section for details on the SMACC-based endmember extraction) as analogues for pure, non-mixed spectra. Based on the similarity between pixel spectra and endmember spectra we calculated the best fit for robust class discrimination. It turns out, that the four extracted endmembers relate to specific material domains, which are mapped in Figure 3B. Corresponding endmember spectra are given in Figure 3C. As a first attempt, we evaluate the endmember contribution to each pixel in the LIF map (Figure 3B) using selected characteristic features and the visualize the feature significance using the false color RGB approach based on LIF signal intensities at the decisive wavelength positions: red (R) at 625 nm, green (G) at 562 nm and blue (B) at 597 nm. Pixels showing LIF spectra with highest similarity to the blue color-coded endmember class (dominated by a spectral peak at the B-position together with notable intensity at the G-position, but weak emission at the R-position, denoted "REE luminescence" in Figure 3C) then appear as bright blueish pixels in the map, whereas pixels with LIF spectra dominated by the red color-coded endmember class (dominated by a broad band covering R- and B-positions, but weak emission at the G-position, denoted "Mineral luminescence") appear as reddish pixels in the map. Finally, the sample edge has been found to be dominated by a spectral shape rising toward the shorter wavelengths, resulting in strongest intensity at the G-position, thus the corresponding pixels are of a green shade. The spatial distribution of the blueish REE luminescence class agrees with the apatite abundance detected in reflectance HSI and MLA (Figures 1C and 3A), coinciding with the Nd absorption feature map (Figure 1D), thus indicating successful REE detection by the LIF mapping and analysis procedure.

The LIF-based REE luminescence class (light-blue color in Figure 3B) confirms results from reflectance HSI and agrees to apatite abundance in the MLA map (Figure 3A). The REE luminescence (Figure 3C) is characterized by four main emission bands represented by dominant sharp peaks that are partly broadened by spectral shoulders. The dominant emission bands can be assigned to Sm^{3+} [21, 24, 44]. The emission bands recorded at 563 nm, 600 nm, 647 nm, and 710 nm are assigned to the electronic transitions $^4G_{5/2} \rightarrow {}^6H_{5/2}$, $^4G_{5/2} \rightarrow {}^6H_{7/2}$, $^4G_{5/2} \rightarrow {}^6H_{9/2}$, and $^4G_{5/2} \rightarrow {}^6H_{11/2}$ respectively [20, 21, 45]. According to ICP-MS results (Table 4), the sample FI17-GU06 has a Sm concentration of 23.7 ppm. The spectral shoulders evident in the second and third band at 600 nm and 647 nm, respectively, indicate the contribution of emission bands from further REE. Their identification is ambiguous due to overlapping fingerprint positions and limited spectral resolution. Hence, selective REE excitation will be beneficial to provide additional information.

The mineral luminescence (red class in Figure 3B,C) is characterized by a broad-band emission stretching from 550 nm to 700 nm. According to Gaft et al. [21] such broad-band red luminescence could be related to Mn^{2+}-activated calcite. The class dominates the LIF map and did indeed match the distribution of calcite as seen from the MLA map (Figure 3A). Detailed comparison suggests that the calcite-associated luminescence covers the dispersed smaller dolomite inclusions. Larger dolomite inclusions appear dark in LIF mapping results and are thus categorized into the background noise class.

The bias between calcite and dolomite abundance suggests that the spatial resolution of the detector limits the detection of smaller crystals or inclusions especially when the mineral shows no specific luminescence. In this case, the effect of spectral mixing results in the prevalence of the luminescent calcite, while the non-luminescent dolomite remains without spectral representation. No characteristic REE fingerprints with typical narrow emission bands are detected in spectra of the mineral luminescence class nor the background noise class. Consequently, LIF mapping results confirm apatite as host for the REE in our FI17-GU06 sample and provide no indication of REE abundance in calcite nor dolomite. Although potential REE luminescence could be quenched by (defects in) the complex host matrix of natural rocks, cross-checking of HSI reflectance data (Figure 1C,D) showed also no indication of REE-related absorption features outside the apatite mineral domain.

The last LIF class represents a strong and very broad band emission in the short-wavelength range without any specific feature (green class in Figure 3B,C). The class is restricted to the sample's edges. The recorded LIF signal might originate from excitation light being strongly scattered at the sample edges or from luminescence of the epoxy resin that the sample is attached with to the glass carrier. As it is only affecting the edges of the sample, it has no influence on the mapping result itself. The class is not further considered.

2.4 | Selective REE Excitation

The above described LIF results successfully identified a REE-related spectral class with a decisive pattern of emission bands. However, the co-existence of multiple REE, either dominated by LREE (sample FI17-GU06) or by HREE (sample NA-RB03), results in major emissions dominating the spectra, while the contributing REE emission bands seen in broadened peaks, double peaks, or peak shoulders remain ambiguous. Therefore, we investigate the capacities of selective REE excitation at 405 nm, 447 nm, and 520 nm for delivering additional information and hence, refining or confirming the identification of individual REEs contained in samples. In the following, we analyze the LIF mapping results for each excitation wavelength separately.

We mapped the maximum signal intensity position in form of an inverted minimum wavelength (MWL) mapping approach (based on tools implemented in hylite, [46], see Experimental Section) for an overview on dominating main peak positions per pixel and comparison of position and/or intensity shifts that could relate to e.g., changes in the mineral host or REE contribution. For the detailed spectral analysis, we focus solely on the REE luminescence class pixels that were identified using the above described approach of endmember extraction and classification. The REE class pixel spectra were then analyzed for peak positions and assigned to potential REE of matching fingerprint positions according to [13, 21, 24]. Additional REE candidates of nearby wavelength position are also considered and evaluated based on comparison to ICP-MS results.

Siilinjärvi sample FI17-GU06

For the sample FI17-GU06 from Siilinjärvi, Finland, the MWL maps resulting from selective excitation document a clear differentiation between REE-containing pixels and sample pixels without REE signals (Figures 4, 5, and 6). The brightness changes indicate significant signal intensity variations, while the predominant color teal indicates a stable maximum intensity wavelength position. Comparing the spatial distribution of these pixels with previous results from MLA and reflectance HSI confirms the correlation with apatite occurrence. The selective excitation MWL maps yield only slight variations in spatial distribution and in dominating peak intensities, especially for the smaller inclusions and along REE domain boundaries. Few red and violet pixels apparent outside of the REE luminescence domain represent overall low signal spectra influenced by noise in the region of increasing mineral matrix luminescence in the chosen wavelength range.

The 405 nm excitation yielded a consistent maximum signal intensity at around 600 nm in the MWL map (Figure 4 left). Based on the SMACC endmember extraction and classification (Figure 4 middle), we could determine corresponding REE class pixels for subsequent fingerprint assignment (Figure 4 right). The spectral range at wavelengths shorter than 600 nm shows extremely variable signal intensities with overall shapes that resemble the LIF class of epoxy/ glass luminescence (cf. Figure 3C). Nevertheless, the classification approach is still able to recognize the REE-class specific pattern of four main emission bands despite the spectral mixing of the two classes.

Using the 405 nm excitation enables the detection of the four main bands at 563 nm, 598, 644, and 704 nm that agree in wavelength position and relative intensity pattern to characteristic Sm^{3+} luminescence [13, 21, 24]. For the 563 nm emission band, neighboring REE fingerprints of Dy^{3+} and Tb^{3+} lie at about 10 nm shorter and longer wavelengths, respectively. Referring to their ICP-MS-based concentrations in this sample (Dy^{3+}: 7.5 ppm; Tb^{3+}: 1.7 ppm, cf. Table 4), we assume that from the two HREE representatives Dy^{3+} potentially contributes to this emission band, while we interpret minor influences from Tb^{3+}. The most intense Sm^{3+}-related emission band at 597 nm overlaps with two bands of Eu^{3+} fingerprint positions at slightly shorter wavelengths roughly -5 and -10 nm). Additionally, the spectral pattern shows a ca. 10 nm wide spectral shoulder at the longer wavelength side. Whether this results from a host-induced fingerprint shift of the Sm-Eu combined emissions or indicates Sm to inhibit different luminescent centers in the crystal with one center responsible for a 597 nm emission and the other one for a 607 nm emission as observed for apatite (e.g., [21, 26]) remains unresolved. The third Sm^{3+}-associated emission band observed at 644 nm coincides with fingerprint positions of Pr^{3+} and of Tb^{3+}, both in the range of less than 5 nm deviation. The Pr^{3+} concentration measured by ICP-MS clearly exceeds the concentration of Sm^{3+} and hence, likely contributes to the observed emission. The spectral shoulder at 649 nm marks an additional emission. The observed pattern suggests that the detector and parameters in use are able to distinguish closely positioned peaks under suitable conditions. The shoulder position at 649 nm agrees with the fingerprint position of Eu^{3+}. A contribution from a neighboring Dy^{3+} emission band at about 10 nm longer wavelength is possible. The last main Sm^{3+}-assigned emission band at 704 nm is less prominent, but still about two times above the standard deviation of the background noise. The peak shows an unspecific, flat top that indicates close-by emission bands with similar intensities and/or overlapping effects. The detected position agrees with a fingerprint of Tb^{3+}. Also Eu^{3+} has a characteristic emission band at around 700 nm.

From the above observations, it becomes clear that REE-attribution based on single emission lines is non-trivial. A more reliable REE assignment needs to be based on multiple positions and their relative intensity patterns compared to reported observations in comparable rock assemblages and host minerals. The REEs Eu^{3+}, Dy^{3+}, and Tb^{3+} were repeatedly considered as contributing to our recorded spectra. The contribution from Eu^{3+} is indicated for three emission positions with matching fingerprints at 593 nm ($^5D_0 \rightarrow {}^7F_1$ transition), 652 nm ($^5D_0 \rightarrow {}^7F_3$

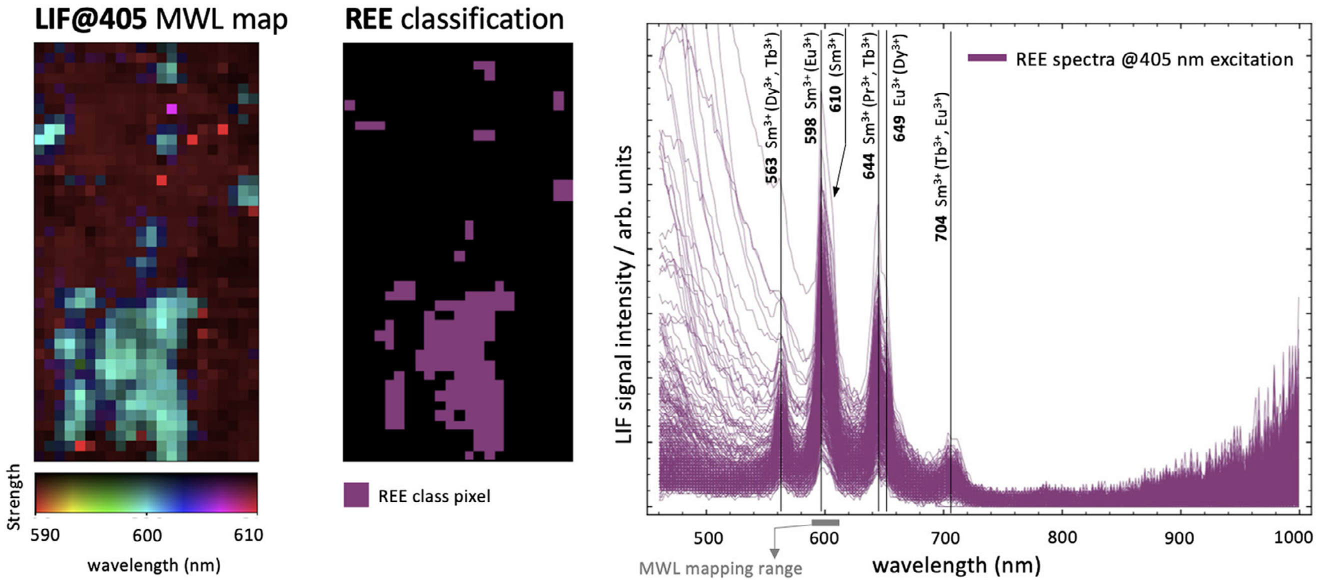

FIGURE 4 | LIF mapping results for selective excitation at 405 nm applied to sample FI17-GU06 from Siilinjärvi, Finland. Left: Minimum wavelengths (MWL) map adapted for detecting position of maximum LIF signal intensity in the range 590 – 610 nm. Middle: REE classification map showing the spatial distribution of REE-containing pixels based on the SMACC algorithm. Right: LIF spectra representing all 456 REE-class pixels. LIF peaks are described by observed wavelength position in nm, associated REE including potentially contributing REEs with slightly deviating fingerprint positions in parentheses.

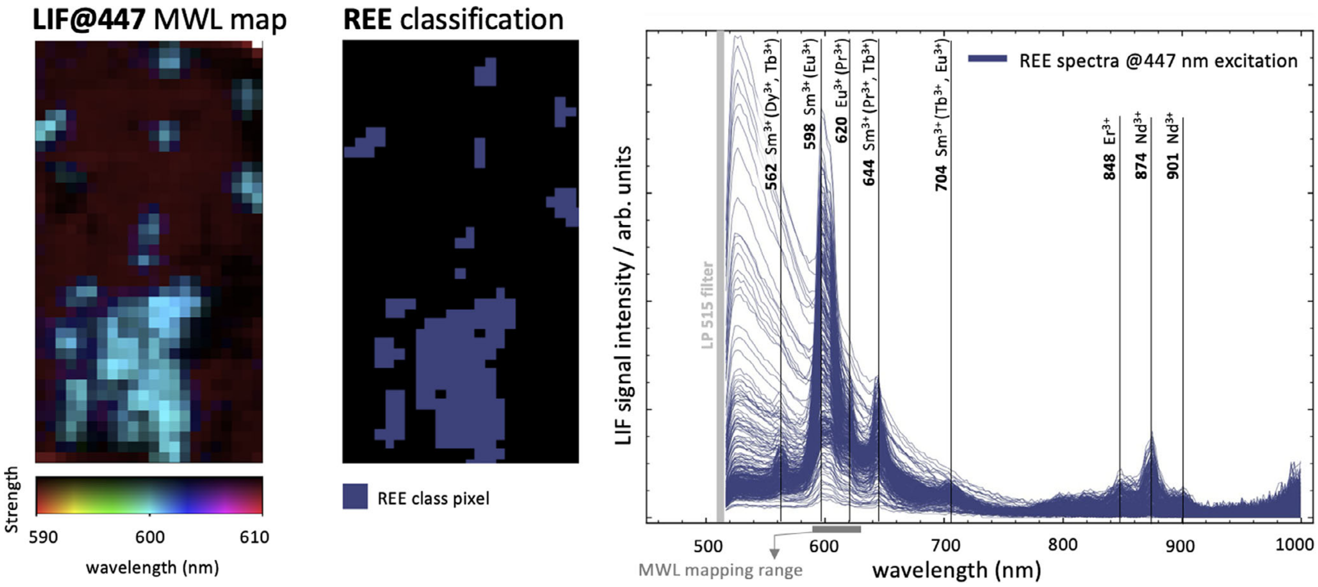

FIGURE 5 | LIF mapping results for selective excitation at 447 nm applied to sample FI17-GU06 from Siilinjärvi, Finland. Left: Minimum wavelengths (MWL) map adapted for detecting position of maximum LIF signal intensity in the range 590 – 610 nm. Middle: REE classification map showing the spatial distribution of REE-containing pixels based on the SMACC algorithm. Right: LIF spectra representing all 308 REE-class pixels. LIF peaks are described by observed wavelength position in nm, associated REE including potentially contributing REEs with slightly deviating fingerprint positions in parentheses.

transition) and 700 nm ($^5D_0 \rightarrow {}^7F_4$ transition) [20, 21, 24]. The usually weak Eu^{3+} emissions at 812 to 832 nm ($^5D_0 \rightarrow {}^7F_6$ transition) are too weak and potentially hidden in the noise at long wavelengths. The typically strong Eu^{3+} transition $^5D_0 \rightarrow {}^7F_2$ around 615 nm [47] is hard to distinguish separately between the prominent Sm^{3+}-related bands at 597 and 644 nm. It might be masked by the dominant Sm^{3+} $^4G_{5/2} \rightarrow {}^6H_{7/2}$ transition or suppressed by energy transfer mechanisms with Sm^{3+} as acceptor of electrons from Eu^{3+}. An emission contribution from Tb^{3+} is potentially related to three fingerprint positions, at 544 nm ($^5D_4 \rightarrow {}^7F_5$ transition), at 645 nm ($^5D_4 \rightarrow {}^7F_2$ transition) and at 703 nm ($^5D_4 \rightarrow {}^7F_0$ transition) [20, 21, 24]. However, other

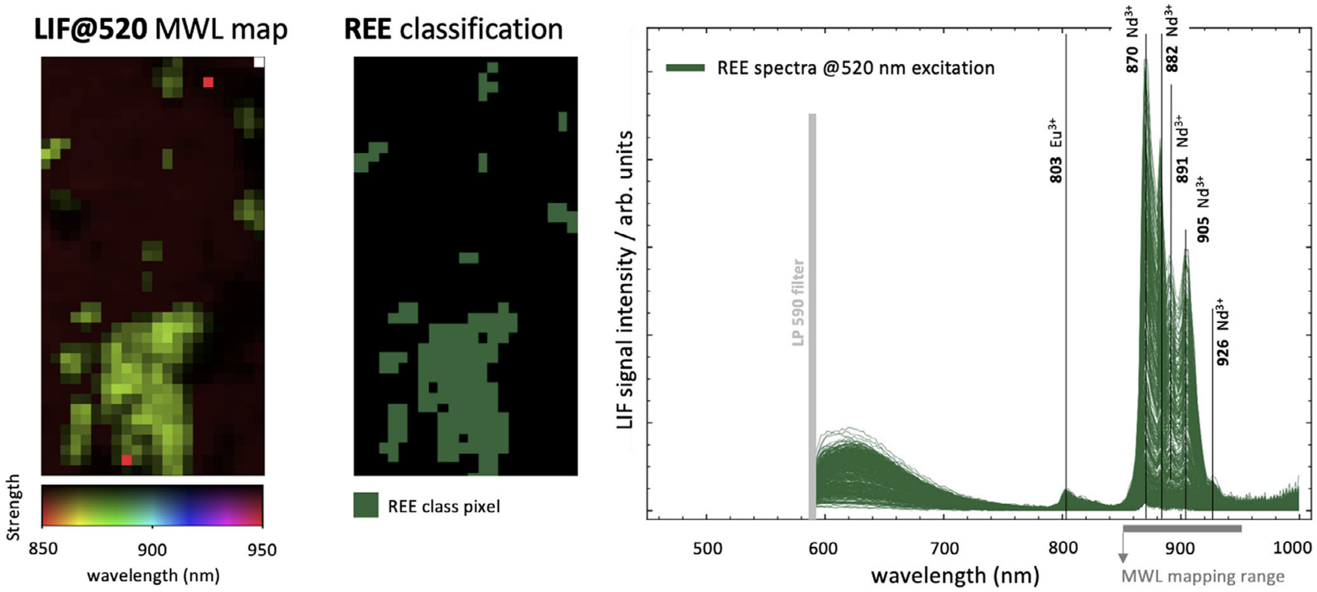

FIGURE 6 | LIF mapping results for selective excitation at 520 nm applied to sample FI17-GU06 from Siilinjärvi, Finland. Left: Minimum wavelengths (MWL) map adapted for detecting position of maximum LIF signal intensity in the range 850 – 950 nm. Middle: REE classification map showing the spatial distribution of REE-containing pixels based on the SMACC algorithm. Right: LIF spectra representing all 308 REE-class pixels. LIF peaks are described by observed wavelength position in nm and associated REE. REE fingerprint emissions are not observed at wavelengths shorter than 800 nm when selecting 520 nm excitation.

characteristic bands are not evident and the low ICP-MS-based Tb concentration of the sample together with typically weak emission bands at wavelengths longer than 550 nm suggests an overall low spectral contribution in REE class spectra. The potential detection of Dy^{3+} is based on two emission bands at 574 nm ($^4F_{9/2} \rightarrow {}^6H_{13/2}$ transition) and at 662 nm ($^4F_{9/2} \rightarrow {}^6H_{11/2}$ transition) [20, 21, 24]. The earlier fingerprint represents the most prominent Dy^{3+} emission band, while the latter is typically of low intensity. The other typically prominent Dy^{3+} emission at 485 nm is not evident in the recorded spectra.

Examining the results from 447 nm excitation and REE classification reveals a slightly increased spatial abundance compared to the 405 nm excitation (Figure 4 left and middle). The detection wavelength range is cut by the long pass filter at 515 nm limiting analysis to longer wavelengths. The dominance of the intense Sm^{3+}-related emission at 598 nm increases (Figure 4 right). Also its spectral shoulder at around 610 nm becomes more prominent resulting in a double-feature appearance of the emission band. Additionally, a second shoulder occurs at 620 nm. The position agrees with an Eu^{3+} fingerprint that was potentially masked in the above 405 nm LIF spectra (cf. Figure 4 right). The fingerprint position of Pr^{3+} at 617 nm (($^3P_1$,$^3P_0$) $\rightarrow$ $^3H_6$ transition) [21, 24] also agrees with the second shoulder position. ICP-MS analysis supports the assignment of the LREE Pr^{3+} (39.5 ppm), as well as Eu^{3+} (6.0 ppm, cf. Table 4). The other three main emission bands decrease in relative intensities, most significantly observed for the emission at 562 nm. Considering a highly efficient excitation of Sm^{3+} in the blue range, represented here in our study by the 447 nm LIF unit, we assume especially Dy^{3+} and Tb^{3+} to respond in a less intense manner. This corresponds to the similarly decreased relative intensities of the emissions at 644 and 704 nm. The luminescence band at 649 nm becomes to weak for robust detection.

An altered excitation selectivity is documented by three new REE emission bands. The emission at 848 nm coincides with the fingerprint position of Er^{3+} ($^4S_{3/2} \rightarrow {}^4I_{9/2}$ transition) reported as a triplet at 842, 850, and 855 nm [24]. The absence of close-by fingerprints of other REE together with the low ICP-MS-based Er concentration in the sample leads to the assumption of an efficient 447 nm excitation of Er^{3+} in this sample, potentially originating from direct absorption into its $^4F_{3/2,5/2}$ levels. Characteristic Nd^{3+} emission bands are detected in the range from 874 to 901 nm ($^4F_{3/2} \rightarrow {}^4I_{9/2}$ transition). Comparing the relatively lower Nd^{3+}-related peak intensities with the prominent main peak of Sm^{3+} contrasts the about 50 times higher ICP-MS-based concentration of Nd (156.5 ppm) in the sample. This observation indicates a non-optimal excitation efficiency for Nd^{3+}.

The 520 nm excitation is accompanied by another detection range reduction leaving an analytical window from 590 to 1000 nm. The observed spectral pattern changes significantly (Figure 6 right). All REE-related features at wavelengths shorter than 780 nm disappear or are completely masked by an unspecific broad luminescence between 600 nm and 660 nm. Instead, a prominent emission band cluster around 900 nm characterises the REE class spectra. This typical cluster is associated to Nd^{3+}. The high signal intensity, especially compared to the previously obtained results, demonstrates a high excitation efficiency for Nd^{3+} using the 520 nm LIF unit. The detected cluster comprises five separate emission bands at 870 nm, 882 nm, 891 nm, 905 nm, and 926 nm. All five bands are attributed to the transition $^4F_{3/2} \rightarrow {}^4I_{9/2}$, stated already above and agree with reported emission band splitting [24]. A single, much weaker emission can be distinguished at 803 nm, which potentially originates from Eu^{3+}. However, typically reported fingerprint positions are around 812 and 832 nm ($^5D_0 \rightarrow {}^7F_6$) and hence, the assignment remains uncertain [21, 24].

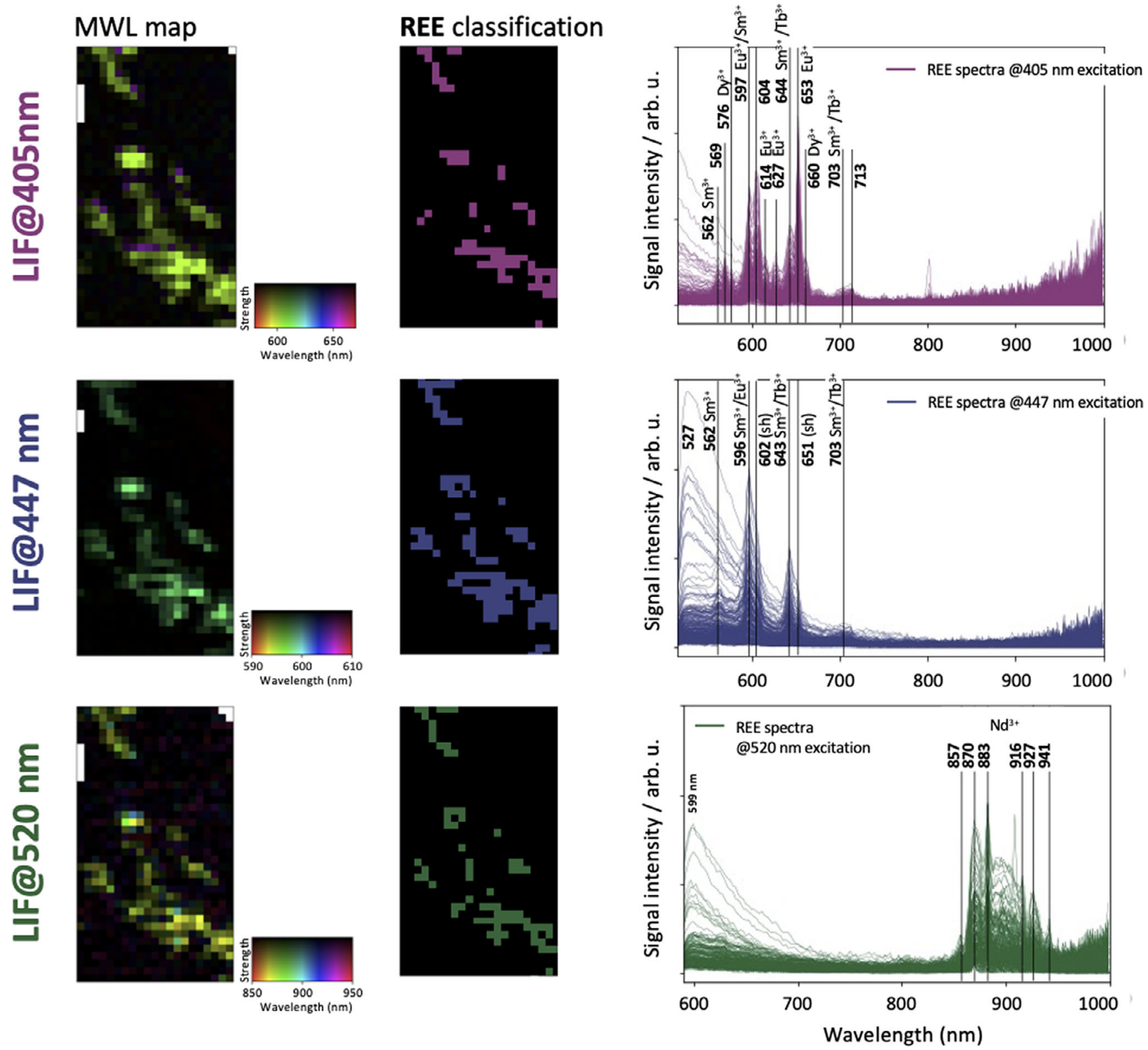

FIGURE 7 | LIF mapping results for selective excitation at 405, 447, and 520 nm applied to sample NA-RB03 from Lofdal, Namibia. Left: Minimum wavelengths (MWL) maps adapted for detecting position of maximum LIF signal intensity in specified ranges (see legend). Middle: REE classification maps showing the spatial distribution of REE-containing pixels based on the SMACC algorithm. Right: LIF spectra representing all detected REE-class pixels. LIF peaks are described by observed wavelength position in nm and associated REE. sh: shoulder.

Lofdal sample NA-RB03

For evaluating the performance of LIF line-scan results from the HREE-enriched sample NA-RB03, originating from Lofdal, Namibia, we focus on the general spectral patterns and outline specific differences to the above described results from the predominantly LREE-containing sample (FI17-GU06). We note that this sample NA-RB03 has similarly high (or higher) LREE concentrations, while HREE concentrations are much higher compared to the previous sample (cf. Table 4). Overall, the selective LIF mapping was also successful for NA-RB03, as shown in Figure 7. Identified REE emission bands agree to transitions described above for the sample FI17-GU06 and are here only given with respect to observation, position and relative intensities. Dependent on the excitation wavelength, major intense emission bands lie at around 600 nm, 650 nm, and 900 nm. The MWL maps indicate a relatively stable position of associated maximum signal intensities within each corresponding spectral range (see legend wavelength range in Figure 7 left). Nevertheless, the MWL map excited at 405 nm reveals few pixels, where the maximum signal intensity shifts from the prevalent 600 nm to around 650 nm indicating a changed intensity ratio. Also results from 520 nm excitation show slight variations of main peak position, likely due to the cluster of bands with comparable intensities (Figure 7 bottom right). The spatial distribution of detected REE class pixels confirms the indication from reflectance HSI-based REE mapping that could only resolve very weak absorptions (cf. Figure 2C). The LIF-based mapping enabled the recording of multiple clear emission bands that are available for an enhanced REE identification and hence, robustness.

REE class spectra excited at 405 nm (Figure 4 right) show more distinct patterns compared to results from the sample FI17-GU06. Again, four major bands are detectable, but contributing emission bands are more distinct and separated from one-another. The four Sm^{3+}-related emission bands at 562 nm, 597 nm, 644 nm, and 703 nm show a decreased relative intensity. An additional emission occurs as a prominent band at 604 nm and could indicate a line splitting from Sm^{3+} or Eu^{3+}. The sample spectra further suggest a more significant contribution from Eu^{3+}, especially evidenced by the prominent emission band at 653 nm. Other Eu^{3+}-related emissions are detectable at 614 nm and 627 nm. Two emission positions at 576 nm and 660 nm agree with Dy^{3+} fingerprints. The indication of Tb^{3+} remains uncertain due to overlapping emission bands with Sm^{3+} positions. We infer no clear spectral dominance of HREE, but note the distinct resolution of multiple emission lines as a robust and rich source for REE assignment.

The excitation at 447 nm reduces the distinctness and number of emission bands (Figure 4 middle). The efficient excitation of Sm^{3+} results in a dominance of the four related emission bands, while separate bands from other REE vanish into shoulders or are completely masked. The contributions from Eu^{3+} and Tb^{3+} to coinciding positions with Sm^{3+} bands is possible, but lacks further evidence. Emission fingerprints of Er^{3+} are not observed despite the efficient excitation at 447 nm and the ca 100 times higher ICP-MS-detected Er concentration of this sample. We assume an energy transfer suppressing Er fingerprint emissions and corresponding enhancement of observed emission bands.

LIF spectra excited at 520 nm enable the detection of the prominent Nd^{3+}-related emission cluster around 900 nm. The most intense emission is recorded at 883 nm in form of a narrow band. The other bands are less confined and range from 870 to 941 nm with declining intensity. The shape of this emission cluster was reported to be characteristic of specific mineral host types (cf. [13]) and matches here with patterns found in phosphate minerals, of which apatite is a representative candidate.

2.5 | Evaluation of Potentials and Limits

Summarizing our results from the integrated reflectance HSI - LIF line-scan setup, we identify two major aspects that outline key potentials and limits, (a) the accurate integrated mapping of minerals and REE abundances including the identification of individual REE representatives (especially representatives of LREE versus HREE), and (b) the efficiency versus resolution/information depth trade-off.

An accurate mapping of mineral domains was achieved using the reflectance HSI data acquired in the VNIR range. Although this spectral range is not ideal for mineral domain discrimination, our mapping results were able to discriminate the main minerals identified by MLA and document a robust spatial match with the high-resolution MLA maps. The comparison of reflectance HSI with MLA maps indicates an even more precise reflectance-based mineral domain map particularly for the differentiation between calcite and Fe-minerals such as goethite, that can be hidden in mixed MLA-classes and then depends on the preferred class grouping strategy. This outlines the strong potential of a reflectance HSI unit for mineral domain mapping applications as an alternative to time consuming, offline MLA and as the basis for integration with LIF. Although MLA provides spatially much higher-resolved mineral maps with far more information on mineral types, a meaningful interpretation still requires expert knowledge. The same overall spatial pattern and domains are recognized by reflectance HSI connected with a clear gain in efficiency.

Reflectance HSI enabled also the identification of mineral domains containing REE based on band-ratio approaches and mapping of feature depths. We found REE features in the apatite domain with a series of significant LREE in the Siilinjärvi sample FI17-GU06, while features of HREE in the Lofdal sample NA-RB03 are very weak and difficult to discriminate. Nevertheless, the band-ratio approach was still able to exploit the weak features (cf Figure 2) and led to a successful mapping in agreement with identified apatite abundances in this sample. The positions of the weak features agree to fingerprints of (Nd,) Er, Ho, and Dy and hence, indicate the predominance of HREE as expected from ICP-MS results. Because of the low significance of the HREE features, the Lofdal sample exemplifies the need for cross-validation. Here, our integration with LIF mapping provides the needed information and can yield increased confidence and also provide an enhanced identification of contained REE species.

The seamless integration with LIF enables the cross-validation of HSI domain mapping and enhanced REE identification. The endmember extraction approach testified the identification of luminescence domains that were associated with HSI-based mineral domains and could unravel distinct spectral classes of luminescent minerals, non-luminescent minerals, and REE luminescence. The inverted MWL mapping has strong potential for insights into spatial variations of dominant emission bands and hence, allows for further interpretation on host minerals (see peak shifts in MWL maps in Figure 7). The recorded LIF spectra further enable a detailed analysis of REE features that outperforms clearly the abilities of HSI reflectance, especially in the case of the Lofdal sample NA-RB03 with very weak absorption features. Multiple distinct emission bands were recorded that are significantly above the noise of the local background and are available for cross-validation and can complement additional REE detections. The overlap and competition together with energy transfer mechanisms still complicates the clear identification of all REE present in the sample and with potential fingerprint emissions in the detection range (cf. Table 4). Here, more sophisticated optical characterization equipment can still outperform our integrated HSI-LIF approach due to higher power densities as well as higher spatial and spectral resolution. Nevertheless, we emphasise the successful excitation and recording of multiple narrow and distinct emissions from several REEs together in one efficient line scan approach that was not available before.

Time-resolved LIF approaches can further support the suppression of mineral luminescence and differentiation of REE contributions. The technical implementation of the needed complex equipment is, however, more suited for laboratory in-depth analysis, while solutions for large sample volumes and in industrial environments require high throughput and simplified solutions. Our results suggest a sufficient discrimination between REE and non-REE containing pixels, peak intensities are significant above the local noise frequency of the background or matrix luminescence and hence, we argue that the additional hardware complexity connected to time-resolved signal acquisition is not always required. We recommend to use and explore the selective excitation capacities instead. The co-existence of multiple REE implies the potential of energy transfers, altering emission intensity ratios and/or masking some fingerprint emissions. This may sometimes hinder the comprehensive identification of all present REEs. On the other hand, such changes also document effects in the sample's composition, which can be used for interpretation.

The above presented results show a currently lower spatial and spectral resolution of our integrated HSI-LIF line-scan setup compared to MLA or CCD-camera-based analysis. As already discussed extensively above, this results in a higher mixing of spectra and masking of mineral inclusions of small sizes and hence, limits the level of details that can be expected. The spatial resolution of the detector could not be fully utilized, because of the dim luminescence signals at the lower sensitivity range of the detector. The spatial binning enabled the recording of LIF spectra with significant REE signals suitable for identification purposes. This comes at the cost of increasing the minimum detectable material domain size, which was in our study a few mm. Also the boundaries of material domains suffer from spectral mixing as they usually occur independent of pixel boundaries. In the context of spectral mixing, we note the nonetheless successful mapping and identification of mineral domains and REE when employing (inverted) MWL mapping, false color RGB mapping and band-ratio approaches that are useful to highlight specific positions and relative intensities in the spectra as a tailored extraction of the most relevant information from the acquired data. Although reflectance HSI data could have been detected at higher spatial resolution because of the much more intense signals, we explored here in this study specifically the integrated approach with consistent parameters for both line-scan methods.

Classical CCD-camera solutions paired with monochromators and high-resolving gratings are clearly outperforming our recorded LIF data by a higher spectral resolution (laboratory CCD-setup used for single-point LIF: ca. 0.13 nm; LIF line-scan data form sCMOS: ca. 2.5 nm after spectral binning of 4). Such a high spectral resolution enables CCD-camera-based measurements to resolve close-by emission bands, clusters of emission lines, and even splitting into sub-levels. Respective setups typically employ high laser power applied to a small measurement spot achieving orders of magnitude more intense luminescence signals suitable for diverse analysis in material science and physics. The approach is ideally suited for in-depth spectroscopy in laboratory experiments. The drawback compared to our HSI-LIF line-scan setup is the low efficiency and restricted compatibility with in-line sensing applications. The method requires point-wise acquisitions in order to record spectral along with spatial information and precise fine-tuning of the hardware components. Our LIF line-scan solution demonstrated successful excitation of a complete scan line compatible with line-detection systems used in the reflectance HSI field. Despite the lower spectral (and spatial) resolution, the LIF data allowed the detection of multiple emission lines, partly depicting close emission positions in form of double peaks or prominent shoulders. The positions and intensity ratios in the detected spectra agree with spectral patterns recorded by a laboratory CCD-camera based setup and hence, confirm successful application of LIF line-scanning.

The core advantage of our HSI-LIF line-scan setup lies in the increased efficiency and compatibility with in-line acquisition of two data dimensions (mineral domains and REE). Although we discussed above the limits connected to the lower spatial and spectral resolution, the line-scan configuration provides the possibility for continuous recordings, while sample material moves below the sensor system. No time delays result from off-line sample preparation and analysis and information is acquired not only for a bulk or single measurement spot, but for an entire row of pixels. Recorded lines can then be easily stacked to produce maps that cover sample pieces or whole material streams. The simultaneous signal detection across a 25 cm wide line was achieved with an exposure time of 325 ms. For our samples of 2 cm in scan direction, we recorded 25 scan lines in ca. 8 s. Accordingly, the used hardware configuration and acquisition parameters yield an overall scan speed of 0,25 cm per s or 4 s per cm. The employed signal acquisition parameters and resulting signals point at several potential future improvements. The used detector already provides the possibility of an increased spatial and spectral resolution as well as scan speed. We note that changes in one impact the other parameters. Therefore, we suggest the increase of LIF excitation power to represent the highest potential for further method enhancement. A more efficient LIF-based REE excitation results in more intense signals that would then allow reduced spectral or spatial binning or an increased scan speed.

3 | Conclusion

We demonstrated the successful in-line mapping of mineral domains and associated REE distributions using an integrated HSI-LIF line-scan setup. Our results highlight the versatility of the approach and its potential to map REEs in different phases and at different concentrations. This is illustrated by sample-specific differences with LREE enrichment in the case of Siilinjärvi, (Finland) and HREE enrichment in the Lofdal locality (Namibia). It is noteworthy that LIF mapping sensitivity varies depending on the mineral phase but allows detection of concentrations as low as tens of ppm. Our approach was validated with MLA maps displaying the mineralogy of the samples and ICP-MS analyses. We suggest several steps in the proposed set-up. (1) Acquisition of HSI reflectance data in the VNIR range to determine mineral domains. (2) Domain identification and mapping of suitable REE hosts. (3) Selective LIF acquisition with specific laser exitations to refine REE identification of specific types and reduce matrix influences. (4) Cross-validation using the integrated LIF and HSI reflectance data. A complete detection of all the REEs detected by ICP-MS is not possible. Nonetheless, distinct REE species are observed and can serve as key representatives. The acquisition speed is currently limited by the very low luminescence signals, which require highly sensitive HSI detectors. An increase of scan speed could be provided by excitation units of higher power densities in order to increase LIF signal intensities and/ or with the use of more sensitive detectors.

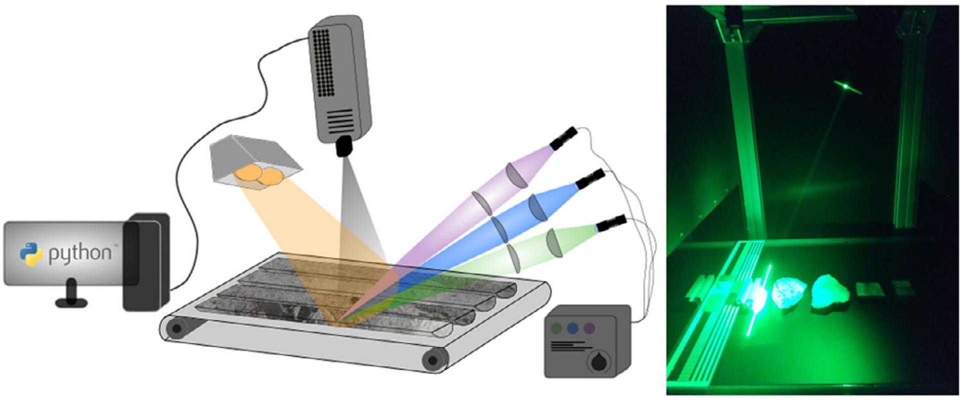

FIGURE 8 | Left: Scheme of the combined line-scan detection system for hyperspectral LIF and reflectance mapping. The joint detector is mounted perpendicular to the sample recording plane (here illustrated as drill-cores on a conveyor belt) with tilted excitation units on both sides, a white light array for reflectance spectroscopy and three LIF excitation units with violet (405 nm), blue (447 nm) and green (520 nm) laser diodes for selective REE excitation. The detection system is linked to a data processing unit, where efficient REE identification and mapping were performed based on in-house developed Python scripts. Right: Photograph of LIF data acquisition using green excitation to scan a series of rock samples.

This approach provides significant efficiency gain compared to offline bulk and pointwise acquisition methods. The proposed workflow address the requirements for an operational transfer into routine industrial applications. This method is of course not meant to compete with or replace lab-based instruments and this field will continue to require research, especially for time-resolved fluorescence. Robust mapping results could be achieve at a scan speed of 4 cm s^{-1}.

4 | Experimental Section

4.1 | Concept of the Line-Scan Setup for LIF and HSI Imaging

Our LIF-HSI line-scan setup consists of (1) an illumination system with (a) three LIF excitation units and (b) a halogen lamp-based white light illumination for reflectance excitation, (2) a free light path to the sample surface and (3) a hyperspectral imaging detector to record both LIF and reflectance signals (see Figure 8). The setup resembles laboratory scan systems with a horizontal scan-surface moving in a given direction, perpendicular-facing detector(s) and slightly tilted illumination. The perpendicular-detector geometry minimizes distortions during imaging of planar samples, whereas the tilting of the illumination did not affect scan geometry, but rather impacts only excitation energy density. While various systems existed for line-scanning HSI in the field of mineral mapping, our integrated experimental setup added a novel, on-purpose-designed LIF excitation module comprising three deliberately chosen laser diodes and, for the seamless integration of both methods, employed a highly light-sensitive hyperspectral line detector that was capable of recording signals from both methods, reflectance, and emission spectroscopy.

4.2 | Single-Point LIF Spectroscopy Lab Setup

In a laboratory set-up for complementary single-point LIF spectroscopy, continuous-wave lasers of fixed wavelengths emitting at 325 nm, at 442 nm (He-Cd laser Kimmon IK 5451 R-E, 14.58 and 16.73 W cm^{-2}) and at 532 nm (LaserQuantum gem532, 26.93 W cm^{-2}) were available. Additionally, we used a laser-driven plasma light source (Energetiq Technology Model EQ-99X LDLS, 220 – 2200 nm) filtered by a monochromator unit (Mountain Photonics Hyperchromator) for more comprehensive excitation spectroscopy. Spectral recordings were done via a 50 cm monochromator unit (Acton SP2560i with a 300 g mm^{-1} grating) combined with a energy-coupled device (CCD) camera (Princeton Instruments SPEC-10:100BR eXcelon, 1340 channels, liquid nitrogen cooled).

TABLE 2 | Technical specifications of the Thorlabs laser diodes used in the LIF excitation unit (information on laser diode model and center wavelength according to manufacturer, power density: measured in the center of the excitation line at focus position with a Thorlabs PM100D power meter and an S142C silicon sensor head to represent the actual energy delivered to the sample surface).

Laser diode	Center wavelength nm	Power density W cm^{-2}
L405P150	405	0.025
L450G1	447	0.830
L520G1	520	0.417

4.3 | LIF Excitation Setup

The LIF units represented a unique prototype jointly developed and then assembled by Freiberg Instruments GmbH. The use of three LIF units allowed for excitation at three different wavelengths, 405 nm at 150 mW optical power, 447 nm at 3000 mW, and 520 nm at 900 mW (see Table 2). The selection of excitation wavelengths resulted from reviewing reported optimized REE excitation energies (see for an overview [21]), own laboratory experiments and matching those with available, powerful laser diode hardware.

Our excitation experiments, conducted in a separate single-point spectroscopy lab setup (see previous sub-section) on another

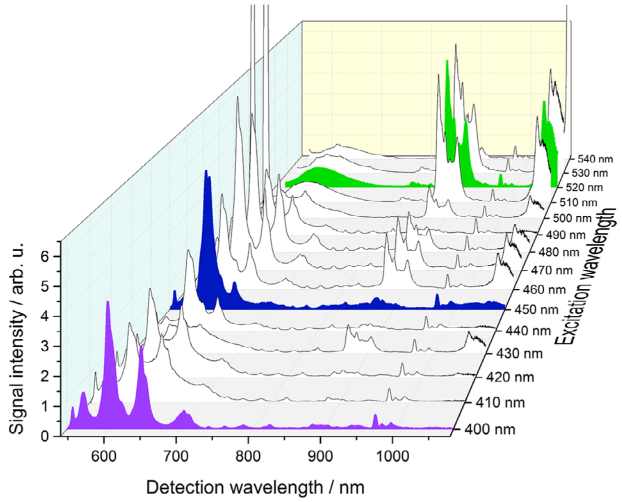

FIGURE 9 | LIF point spectra for a range of excitation wavelengths showing selective excitation of particular REEs by certain excitation wavelengths. The three excitation wavelengths chosen as LIF sources are highlighted.

sample from the Siilinjärvi mine (FI17-RJA-1, not presented in detail here) that resembled the mineralogical composition of sample FI17-GU6. Results confirmed significant changes in the PL spectra with different excitation wavelengths, as shown in Figure 9. Three distinct spectral patterns could be recognized, whose appearance and intensity could be optimized by appropriate excitation wavelength choice. Accordingly, a combination of three excitation wavelengths showed the best match with efficient excitation windows across the entire REE series (see further details on suitable wavelengths for REE excitation in Ref. [24]). The chosen wavelengths reflect a balanced solution for most REEs and furthermore, allow for a selective excitation according to variable user needs. This accounts specifically for the high-energy excitation (violet) required for e.g., Dy, Eu etc. [21, 24], while e.g., Pr and Sm are known to be susceptible especially to blue excitation [32, 48], or Nd known for its sensitivity to green excitation (see [21, 34, 49]). The photograph on the right hand side of Figure 8 depicts the LIF line-scan setup in operation on a conveyor belt system using the 520 nm LIF excitation unit during rock sample scanning.

Generally, high optical power density was required to ensure sufficient excitation power density on the samples, but the high power requirement comes at the cost of thermal stability. Especially the latter two longer-wavelength laser diodes with an optical power of 900 mW or more require a monitoring with photodiodes and cooling with fans in order to avoid spectral shifts of the excitation wavelength during the measurements.

In order to match the LIF excitation geometry with the detector line focus, we developed an optical configuration using cylindrical lenses that transforms the point emission of the laser diodes into a line. The resulting excitation line had a 0.1 cm width at the focus position and a 25 cm length at a working distance of about 47 cm. The excitation line focus was carefully matched to the focus line of the HSI detector (see next section on signal acquisition). The angle of the excitation light path to the sample surface could be adjusted in a range of roughly 45 – 80°.

4.4 | Signal Acquisition for LIF and Hyperspectral Reflectance Spectroscopy

In our integrated setup, LIF and HSI signals from the sample were detected with an sCMOS-CL-50-V10E hyperspectral camera from Specim (Spectral Imaging Oy Ltd., Oulu, Finland). The camera was a pushbroom-type line scan sensor, which made it well-suited for continuous imaging applications for material streams or drill-cores and their material composition mapping. The camera operated 16-bit-based in the VIS/NIR range from 400 to 1000 nm. The sCMOS chip resolved 946 spectral pixels and 2184 spatial pixels (pixel pitch 6.5 μm on chip) resulting in a spectral sampling of 2.54 nm and a spatial sampling of 0.11 mm. With a focal distance of 68 cm (adjustable in a margin of ±1.5 cm), the objective lens from Schneider Kreuznach Xenoplan 2.0/28 provided an effective detection line of approximately 25 cm width.

For LIF signal recordings, suitable optical long-pass (LP) filters were required to exclude scattered illumination light from the detection signal, which contains orders of magnitude less intense fluorescence signals. We used filters with edge wavelengths at 450 nm, 515 nm, and 590 nm, respectively, to suppress scattered excitation laser light (see Table 2) and hence avoid saturating the detector. As a consequence, recorded sample spectra comprise solely wavelengths longer than the given filter edges up to the detector's limit at 1000 nm. The software to control the LIF unit was developed by Freiberg Instruments GmbH whereas the conveyor belt control software was an in-house development.

The same detection conditions were used for reflectance HSI spectroscopy to simplify data integration. In particular, the same integration time, frame rate, spatial binning and belt speed yield pixel sizes matching LIF data, making any comparison or data fusion more straightforward. The required homogeneous white light illumination was achieved with broad-band quartz-tungsten halogen units that delivered a continuous illumination in the VIS-NIR covering the entire detection range of the sCMOS camera. The light sources were arranged in an array of eight bulbs for spatially homogeneous illumination intensities across the detection line of 25 cm length. White, grey, and black reference panels (PTFE, >99 %, 50 %, and 6 % reflectance, respectively) were included in each measurement scene along with a dark image taken with a closed shutter of the camera, for converting recorded data to reflectance values. All measurements were performed at room temperature and after an initial time delay to reach thermal stability of the light sources. The measurements were carried out in a dark-lab environment, where all artificial light sources were switched off and natural daylight was excluded.

4.5 | Data Description

We used the acquisition software LUMO (LUMO Scanner, version 2018-5, Spectral Imaging Oy Ltd, Oulu, Finland) to operate the camera and record the signals using the above mentioned parameters for excitation/ illumination, detection, and belt speed. The data output from the sCMOS sensor ImSpector V10E represented an HSI data cube containing the series of recorded scan lines, which were stacked to form LIF and HSI maps. The number of lines recorded one after the other was chosen to capture the entire sample dimensions. In our dynamic setup, the combination of 325 ms integration times per line, a belt speed of 0.5 cm s^{-1} and a frame rate of 3 Hz allowed for geometrically non-distorted sample scans with most prominent LIF signals. Each line was, accordingly, a single recording over the integration time of 325 ms and each pixel therein then represented a full VNIR spectrum documenting the emitted energy sum during the 325 ms.

Appropriate LIF signal acquisition involved a trade-off between conveyor belt speed and detector settings for sufficient signal-to-noise ratios in order to ensure robust REE identification and mapping. The acquisition of stable signals from the very dim luminescence signals demands for sufficient photon counts per scanned spatial unit (pixel) and spectral unit (band). We applied a spatial binning of eight and spectral binning of four in order to achieve more robust signals and still preserve the spectral information associated with REE fingerprints. Resulting HSI data cubes then contain 273 spatial pixels per line (after binning of eight for the total line with 2184 pixel) with 236 spectral bands per spatial pixel. The pixel number per line together with the 25 cm width of the scan line determines a pixel size of 0.9 mm.

We scanned two representative samples, FI17-GU06 and NA-RB03, with the dimensions of 4 cm x 2 cm. For each sample, we acquired one HSI data cube for reflectance spectroscopy and four scans for LIF spectroscopy, where one represents excitation signals from a combined 405 nm plus 447 nm excitation in order to maximise stimulation power density applied to the sample surface. The three remaining LIF data cubes were retrieved from separate scans using each of the three individual LIF units. Cropping the scanned data cubes to the sample dimension yields sample data with ca. 25 scan lines of ca. 45 sample pixels and a corresponding total pixel count of 1125 per sample. Robust LiF peaks correspond to a signal-to-noise-ratio (S/N) of 340:1 calculated for the radiance data in use. Nevertheless, we also observed weak signals, which were associated to REE occurrences. Therefore, we included all peaks detected above the local frequency noise (one standard deviation) apparent in the spectral region of interest. Associated peak detection was then based on a polynominal fit in order to reduce potential bias from spectral sampling of the detector.

4.6 | Data Pre-Processing

Pre-processing of the acquired HSI data cubes was done in the sCMOS-control software LUMO (Spectral Imaging Ltd., Oulu Finland). The LUMO software internally converted the measured raw digital numbers seen by the sensor into radiance information and removed known dead pixels using camera-specific calibration files from the manufacturer. After this pre-processing step, the exported radiance data was available for further processing in Python (see section on data processing).

4.7 | Data Processing for LIF and HSI Reflectance Mapping

We processed the recorded hyperspectral data cubes using the open source programming environment Python 3.6 [50] for transparent, traceable, and reproducible data handling. For the newly generated LIF hyperspectral data cubes, we developed own, in-house processing and visualisation routines. For this, we employed tools from the comprehensive Python toolbox hylite 1.36 [46]. It originally was developed for reflectance data cubes, but its efficient solutions for hyperspectral data cubes in general could be nicely adjusted to and combined with solutions for the specific needs of LIF spectroscopic analysis.

While LIF acquisitions were analyzed at the radiance level, reflectance spectroscopy measurements required conversion from radiance to reflectance. To achieve this, we linearly adjusted the data by fitting the in-scene acquired calibration targets to their known reference reflectance spectrum (Emprical Line Correction). This correction was done line-wise to compensate for any across-track illumination variations. Afterward, the data was cropped to the sample region of interest.

For basic data visualisation, we used a false-color composite approach with optional normalization and saturation enhancement as implemented in the hylite toolbox. By mapping selected spectral bands to the Red, Green, and Blue channels of the visualisation plot, spatial variations in spectral shape can be highlighted and used to visually discriminate spectral domains of interest. For the characterization of the sample's main spectral components (classes) and their spatial abundance, we applied endmember extraction and spectral classification tools provided by the Sequential Maximum Angle Convex Cone (SMACC) function of the image processing and analysis software ENVI version 4.8 (Exelis Visual Information Solutions, Boulder, Colorado).

The component (class) including REE features was then further analyzed to match detected emission and absorption bands with known diagnostic features (fingerprints) from the literature for the identification of individual REEs (i.e., [13, 21, 24]). For LIF data, we performed an adapted minimum wavelength mapping using the multi-gaussian absorption feature-fitting algorithm implemented in hylite in order to map maximum signal intensities in a given wavelength range. The resulting pseudo-color map indicates spatial variations of selected REE feature position and intensity in high detail.

For the mapping of subtle REE absorption features in reflectance data, we additionally calculated REE band ratio maps. A simple band ratio BR can be designed by

$$BR = (Band_{LeftFeatureShoulder} + Band_{RightFeatureShoulder})/Band_{FeatureCenter}$$

The result could be visualized in pseudo-color to indicate the spatial distribution of the absorption intensity. Several band ratios could be combined to account for materials with multiple indicative features and increase robustness of the detection.

The integration of HSI reflectance and LIF mapping results after sequential acquisition was based on reference markers that define start and end positions. This supported the seamless integration of the two data sets and comparison of respective information. The strategy allowed the co-registration of both data sets and provides the basis for further data fusion and associated analytical methods.

TABLE 3 | Description of samples used to evaluate the performance of our LIF line-scan setup (further details are given in the Supporting Information; lithology and REE minerals according to [53–55, 59, 60], TREO: total rare-earth oxide content given in % as a sum of lanthanides and without Y and Sc based on ICP-MS geochemical analysis).

Sample ID	lithology	REE minerals	TREO content (in %)
Siilinjärvi (Finland)			
FI17-GU06	alkaline carbonatite-glimmerite complex (mainly calcite, accessory fluoroapatite)	xenotime-(Ce), pyrochlore, and strontianite	0.091 (HREE 0.004)
Lofdal (Namibia)			
NA-RB03	alkaline carbonatite complex (Fe-enriched carbonatite dyke generation)	xenotime-(Y), synchysite-(Ce), monazite (Ce)	0.375 (HREE 0.277)

TABLE 4 | REE concentrations in the studied samples FI17-GU06 and NA-RB03 based on ICP-MS geochemical analysis.

REE	La	Ce	Pr	Nd	Sm	Eu	Gd	Tb	Dy	Ho	Er	Tm	Yb	Lu
Concentration (in ppm)														
FI17-GU06	127.0	316.0	39.5	156.5	23.7	6.0	15.0	1.7	7.5	1.2	2.7	0.3	1.5	0.2
NA-RB03	117.0	213.0	24.6	117.5	277	157.5	617	108.5	607.0	111.0	279.0	36.2	191.5	25.3

4.8 | Scanning Electron Microscopy-Based Mineral Liberation Analysis (SEM-MLA)

For independent result validation, we performed scanning electron microscopy (SEM)-based mineral liberation analysis (MLA). Polished thin sections were prepared by cutting representative sample material, followed by grinding and polishing the surface area, and then applying a thin carbon coating to prevent surface charging during data acquisition. Automated MLA analysis was carried out using a FEI Quanta 650 F field emission SEM instrument (FEI, Hillsboro, OR, USA), equipped with two Bruker Quantax X-Flash 5030 energy dispersive X-ray detectors (EDX, Bruker, Billerica, MA, USA). The mineralogical information was collected by grain-based X-ray mapping mode (GXMAP). This mapping mode involved the acceleration of the electron beam by a voltage of 25 kV, resulting in a 10 nA probe current. The settings of mapping frames yielded a spatial raster with X-ray measurement results every 40 μm. The MLA 3.1.4 software package was used for semi-automated data acquisition [51], as well as for MLA data processing and evaluation.

5 | Material

To investigate the performance of the joint LIF-reflectance line-scan setup, we used REE-bearing rocks from two well studied independent REE deposits, the Siilinjärvi site in Finland and the Lofdal site in Namibia. Both were carbonatite complexes, but differ in REE concentration, host minerals and dominance of light (LREE) versus heavy REE (HREE).

The first sample represents characteristic rocks that were collected within the active mine area from the Siilinjärvi carbonatite complex in Finland. The complex was composed of an 1.8 Ga old metamorphosed unit of alkaline-carbonatite and glimmerite rocks surrounded by granite gneiss, and intruded by several younger generations of dikes and intrusions e.g., [52, 53]. The main carbonate was calcite, and small amounts of dolomite occur as thin lamellae within the calcite (calcite:dolomite ratio of 4:1). Accessory minerals were fluoroapatite, magnetite, barite, biotite, and zircon e.g., [53–55]. Previous studies mapped the local extents of the main minerals and their associations by UAV HSI measurements [56], and demonstrated successful identification of areas containing REEs based on the diagnostic absorption features of Nd [18]. The deposit was currently mined for apatite to produce phosphate, but the deposit contains also an unexploited REE content e.g., [55]. The apatite reaches concentrations of up to 25 % in the carbonatite, with crystal sizes of millimeters to decimeters e.g., [53]. Significant apatite content was also found in the glimmerite [57].

The average REE content in apatite was reported to be 0.4% [54]. Other major REE-hosting minerals comprise monazite-(Ce), pyrochlore-group minerals, LREE-bearing strontianite and REE-bearing Ti, Nb-phases e.g., [55]. Geochemical analysis of those minerals identified a dominance of Ce, Nd, La, Sm, and Gd (LREE) among the present REE [58]. Tables 3 and 4 present inductively coupled plasma mass spectrometry (ICP-MS) data for the representative sample FI17-GU06, showing the total REE content and detailed REE composition, respectively.

The second sampling site represents the characteristic carbonate rocks from the Lofdal Alkaline Carbonatite Complex in the north-western part of Namibia. The Lofdal Complex was ideal for complementing our tests of the LIF line-scan setup because of the carbonatite's unusually high enrichment in HREEs compared to the less concentrated LREEs [59]. The Lofdal site comprises an about 750 Ma old intrusive complex within the paleo-proterozoic basement complex. It consisted of the main syenite-carbonatite intrusion and a swarm of SW-NE striking carbonatite dikes and calcite carbonatite plugs combined with phonolite, syenite and mafic dykes and plugs e.g., [14, 59]. Booysen et al. [14] identified two generations of dykes, an iron-enriched generation striking about 35° NE and a less enriched one striking about 60° NE and locally cross-cutting the previous generation.

Xenotime-(Y) is the dominant HREE host mineral, occurs in iron-rich carbonatite dykes and was associated with iron oxides, thorite, apatite and synchysite-(Ce) and monazite (Ce) [59, 60]. Representative samples from both dyke generation indicate 21 % Fe and 0.9 % Y versus 2.5 % Fe and 0.5 % Y. The composition confirmed the differentiation into two types and the higher HREE enrichment in the Fe-rich type (taking Y as a proxy for HREE contents in rocks [14]). The sample selected for this study represents the Fe-rich generation of carbonatite dykes. Tables 3 and 4 present inductively coupled plasma mass spectrometry (ICP-MS) data for the representative sample NA-RB03, showing the total REE content and detailed REE composition, respectively.

Acknowledgments

The authors want to thank EIT Raw Materials for funding project inSPECtor (Grant No.16304) - furthermore the companies Freiberg Instruments GmbH and Specim Spectral Imaging Oy Ltd. for technical support and the Geological Survey of Finland GTK for the delivery of sample material.

Open access funding enabled and organized by Projekt DEAL.

Conflicts of Interest

The authors declare no conflicts of interest.

Data Availability Statement

The data that support the findings of this study are available from the corresponding author upon reasonable request.

References

1. V. T. McLemore, “Rare Earth Elements (REE) Deposits in New Mexico,” *2012 SME Annual Meeting and Exhibit 2012, SME 2012, Meeting Preprints, Seattle, Washington, USA* 1 (2012): 707–713.

2. J. H. L. Voncken, *The Rare Earth Elements: An Introduction* (Springer, 2016).

3. A. V. Naumov, “Review of the World Market of Rare-Earth Metals,” *Russian Journal of Non-Ferrous Metals* 49, no. 1 (2008): 14–22.

4. I. B. D. Lima and W. L. Filho, *Rare Earths Industry - Technological, Economic, and Environmental Implications* (Elsevier, 2015).

5. G. Barakos, J. Gutzmer, and H. Mischo, “An Outlook on the Rare Earth Elements Mining Industry,” *AusIMM Bulletin* 2 (2016): 62–66.

6. European Commission, *Report on Critical Raw Materials for the EU: Report of the Ad-hoc Working Group on Defining Critical Raw Materials* (European Commission, 2014).

7. R. N. Clark and A. N. Rencz, *Spectroscopy of Rocks and Minerals and Principles of Spectroscopy* (Wiley, 1999).

8. R. Clark, J. Boardman, J. Mustard, F. Kruse, C. Ong, C. Pieters, and G. Swayze, “Mineral Mapping and Applications of Imaging Spectroscopy,” in *2006 IEEE International Symposium on Geoscience and Remote Sensing* (2006): 1986–1989.

9. F. Kruse, “Identification and Mapping of Minerals in Drill Core Using Hyperspectral Image Analysis of Infrared Reflectance Spectra,” *International Journal of Remote Sensing* 17, no. 9 (1996): 1623–1632.

10. F. Kruse, O. Weatherbee, W. Peppin, R. Bedell, W. Calvin, and J. Taranik, “HSI Mineral Mapping from Airborne, Outcrop, and Drill-Core Perspectives,” *Proceedings of SPIE - The International Society for Optical Engineering* 1 (April 2010): 7687, https://doi.org/10.1117/12.855445.

11. D. J. Turner, B. Rivard, and L. A. Groat, “Visible and Short-Wave Infrared Reflectance Spectroscopy of REE Fluorocarbonates,” *American Mineralogist* 99, no. 7 (2014): 1335–1346.

12. D. J. Turner, “Reflectance Spectroscopy and Imaging Spectroscopy of Rare Earth Element-Bearing Mineral and Rock Samples,” (Ph.D. dissertation, University of British Columbia, 2015).

13. S. Lorenz, J. Beyer, M. Fuchs, P. Seidel, D. Turner, J. Heitmann, and R. Gloaguen, “The Potential of Reflectance and Laser Induced Luminescence Spectroscopy for Near-Field Rare Earth Element Detection in Mineral Exploration,” *Remote Sensing* 11, no. 1 (2019): 1–21.

14. R. Booysen, R. Zimmermann, S. Lorenz, R. Gloaguen, P. A. M. Nex, L. Andreani, and R. Möckel, “Towards Multiscale and Multisource Remote Sensing Mineral Exploration Using RPAS: A Case Study in the Lofdal Carbonatite-Hosted REE Deposit, Namibia,” *Remote Sensing* 11, no. 21 (2019): 2500.

15. R. Zimmermann, M. Brandmeier, L. Andreani, K. Mhopjeni, and R. Gloaguen, “Remote Sensing Exploration of Nb-Ta-LREE-Enriched Carbonatite (Epembe/Namibia),” *Remote Sensing* 8, no. 8 (2016): 620.

16. N. K. Boesche, C. Rogass, C. Lubitz, M. Brell, S. Herrmann, C. Mielke, S. Tonn, O. Appelt, U. Altenberger, and H. Kaufmann, “Hyperspectral REE (Rare Earth Element) Mapping of Outcrops—Applications for Neodymium Detection,” *Remote Sensing* 7, no. 5 (2015): 5160.

17. D. A. Neave, M. Black, T. R. Riley, S. A. Gibson, G. Ferrier, F. Wall, and S. Broom-Fendley, “On the Feasibility of Imaging Carbonatite-Hosted Rare Earth Element Deposits Using Remote Sensing,” *Economic Geology* 111, no. 3 (2016): 641–665.

18. R. Booysen, R. Jackisch, S. Lorenz, R. Zimmermann, M. Kirsch, P. A. M. Nex, and R. Gloaguen, “Detection of REEs with Lightweight UAV-Based Hyperspectral Imaging,” *Scientific Reports* 10 (2020): 17450.

19. S. Asadzadeh, N. Koellner, and S. Chabrillat, “Detecting Rare Earth Elements Using EnMAP Hyperspectral Satellite Data: A Case Study from Mountain Pass, California,” *Scientific Reports* 14 (2024): 20766.

20. G. Dieke, *Spectra and Energy Levels of Rare Earth Ions in Crystals* (Interscience Publishers, 1968).

21. M. Gaft, R. Reisfeld, and G. Panczer, *Modern Luminescence Spectroscopy of Minerals and Materials*, 1st ed (Springer-Verlag, 2005).

22. M. Czaja, S. Bodyl-Gajowska, and Z. G. Mazurak, “Steady-State Luminescence Measurement for Qualitative Identification of Rare Earth Ions in Minerals,” *Journal of Mineralogical and Petrological Sciences* 108 (04 2013): 47–54.

23. P. Seidel, S. Lorenz, T. Heinig, R. Zimmermann, R. Booysen, J. Beyer, J. Heitmann, and R. Gloaguen, “Fast 2D Laser-Induced Fluorescence Spectroscopy Mapping of Rare Earth Elements in Rock Samples,” *Sensors* 19, no. 10 (2019): 2219.

24. M. C. Fuchs, J. Beyer, S. Lorenz, S. Sharma, A. D. Renno, J. Heitmann, and R. Gloaguen, “A Spectral Library for Laser-Induced Fluorescence Analysis as a Tool for Rare Earth Element Identification,” *Earth System Science Data* 13, no. 9 (2021): 4465–4483.

25. M. Gaft and G. Panczer, “Laser-Induced Time-Resolved Luminescence Spectroscopy of Minerals—A Powerful Tool for Studying the Nature of Emission Centres,” *Mineralogy and Petrology* 107 (2013): 363–373.

26. R. Reisfeld, M. Gaft, G. Boulon, C. Panczer, and C. K. Jørgensen, “Laser-Induced Luminescence of Rare-Earth Elements in Natural Fluor-Apatites,” *Journal of Luminescence* 69, no. 5-6 (1996): 343–353.

27. M. Czaja, S. Bodyl-Gajowska, P. Gluchowski, Z. Mazurak, and W. Strek, “Luminescence Properties of Rare Earth Ions in Fluorite, Apatite and Scheelite Mineral,” *Journal of Alloys and Compounds* 451, no. 1 (2008): 290–292.

28. M. Czaja, S. Bodyl-Gajowska, R. Lisiecki, A. Meijerink, and Z. Mazurak, “The Luminescence Properties of Rare-Earth Ions in Natural Fluorite,” *Physics and Chemistry of Minerals* 39, no. 8 (2012): 639–648.

29. S. Romppanen, H. Häkkänen, and S. Kaski, “Laser-Induced Time-Resolved Luminescence in Analysis of Rare Earth Elements in Apatite and Calcite,” *Journal of Luminescence* 233 (2021): 117929.

30. M. Gaft, R. Reisfeld, G. Panczer, G. Boulon, S. Shoval, and B. Champagnon, “Accommodation of Rare-Earths and Manganese by Apatite,” *Optical Materials* 8, no. 1 (1997): 149–156.

31. M. Gaft, G. Panczer, R. Reisfeld, and E. Uspensky, “Laser-Induced Time-Resolved Luminescence as a Tool for Rare-Earth Element Identification in Minerals,” *Physics and Chemistry of Minerals* 28, no. 5 (2001): 347–363.

32. M. Czaja, S. Bodył, R. Lisiecki, and Z. Mazurak, “Luminescence Properties of Pr^{3+} and Sm^{3+} Ions in Natural Apatites,” *Physics and Chemistry of Minerals* 37, no. 7 (2010): 425–433.

33. M. Gaft, R. Reisfeld, G. Panczer, and M. Dimova, “Time-Resolved Laser-Induced Luminescence of UV–Vis Emission of Nd^{3+} in Fluorite, Scheelite and Barite,” *Journal of Alloys and Compounds* 451, no. 1-2 (2008): 56–61.

34. H. Friis, A. A. Finch, C. T. Williams, and J. M. Hanchar, “Photoluminescence of Zircon ($ZrSiO_4$) Doped with REE^{3+} (REE = Pr, Sm, Eu, Gd, Dy, Ho, Er),” *Physics and Chemistry of Minerals* 37, no. 6 (2010): 333–342.

35. H. Broicher, “Bulk Sorting by LIF: Quality Control of Ores for Bulk Sorting and Blending by Laser-Induced Fluorescence Analysis,” *Mining Engineering* 52, no. 9 (September 2000): 24–28.

36. H. F. Broicher, “Dilution Control: Online and Real-Time Recognition of Ore and Waste by LIF,” *SME Annual Meeting* 1 (March 2005): 1–5.

37. K. Nienhaus and A. Bayer, “Innovative Systems for Horizon Control of Mining Machines by Means of Laser-Induced Fluorescence (LIF),” *Mine Planning and Equipment Selection, Kalgoorlie, WA* 1 (January 2003): 1–7.

38. T. Kauppinen, N. Khajehzadeh, and O. Haavisto, “Laser-Induced Fluorescence Images and Raman Spectroscopy Studies on Rapid Scanning of Rock Drillcore Samples,” *International Journal of Mineral Processing* 132 (2014): 26–33.

39. M. Gaft, G. Panczer, E. Uspensky, and R. Reisfeld, “Laser-Induced Time-Resolved Luminescence of Rare-Earth Elements in Scheelite,” *Mineralogical Magazine* 63, no. 2 (1999): 199–210.

40. D. Elson, I. Munro, J. Requejo-Isidro, J. McGinty, C. Dunsby, N. Galletly, G. Stamp, M. Neil, M. Lever, P. Kellett, et al., “Real-Time Time-Domain Fluorescence Lifetime Imaging Including Single-Shot Acquisition with a Segmented Optical Image Intensifier,” *New Journal of Physics* 6, no. 1 (2004): 180.

41. R. Datta, T. M. Heaster, J. T. Sharick, A. A. Gillette, and M. C. Skala, “Fluorescence Lifetime Imaging Microscopy: Fundamentals and Advances in Instrumentation, Analysis, and Applications,” *Journal of Biomedical Optics* 25, no. 7 (2020): 071203–071203.

42. G. A. Waychunas, “Apatite Luminescence,” *Phosphates: Geochemical, Geobiological and Materials Importance* 48 (October 2019): 701–748.

43. S. Yanagida, Y. Hasegawa, K. Murakoshi, Y. Wada, N. Nakashima, and T. Yamanaka, “Strategies for Enhancing Photoluminescence of Nd^{3+} in Liquid Media,” *Coordination Chemistry Reviews* 171 (1998): 461–480.

44. R. Reisfeld, M. Gaft, G. Boulon, C. Panczer, and C. Jørgensen, “Laser-Induced Luminescence of Rare-Earth Elements in Natural Fluor-Apatites,” *Journal of Luminescence* 69 (1996): 343–353.

45. R. Yu, H. M. Noh, B. K. Moon, B. C. Choi, J. H. Jeong, H. S. Lee, K. Jang, and S. S. Yi, “Photoluminescence Characteristics of Sm^{3+} Doped $Ba_3La(PO_4)_3$ as New Orange-Red Emitting Phosphors,” *Journal of Luminescence* 145 (2014): 717–722.

46. S. T. Thiele, S. Lorenz, M. Kirsch, I. Cecilia Contreras Acosta, L. Tusa, E. Herrmann, R. Möckel, and R. Gloaguen, “Multi-Scale, Multi-Sensor Data Integration for Automated 3-D Geological Mapping,” *Ore Geology Reviews* 136 (2021): 104252.

47. T. Jansen, T. Jüstel, M. Kirm, H. Mägi, V. Nagirnyi, E. Tõldsepp, S. Vielhauer, N. Khaidukov, and V. Makhov, “Site Selective, Time and Temperature Dependent Spectroscopy of Eu^{3+} Doped Apatites (Mg, Ca, $Sr)_2Y_8Si_6O_{26}$,” *Journal of Luminescence* 186 (2017): 205–211.

48. M. Gaft, R. Reisfeld, G. Panczer, E. Uspensky, B. Varrel, and G. Boulon, “Luminescence of Pr^{3+} in Minerals,” *Optical Materials* 13, no. 1 (1999): 71–79.

49. C. Lenz, D. Talla, K. Ruschel, R. Škoda, J. Götze, and L. Nasdala, “Factors Affecting the Nd^{3+} (REE^{3+}) Luminescence of Minerals,” *Mineralogy and Petrology* 107, no. 3 (June 2013): 415–428.

50. G. Van Rossum and F. L. Drake Jr, *Python Reference Manual* (Centrum voor Wiskunde en Informatica Amsterdam, 1995).

51. Y. Gu, “Automated Scanning Electron Microscope Based Mineral Liberation Analysis: An Introduction to JKMRC/FEI Mineral Liberation Analyser,” *Journal of Minerals and Materials Characterization and Engineering* 2, no. 1 (2003): 33–41.

52. K. Puustinen, “The Carbonatite of Siilinjärvi in the Precambrian of Eastern Finland: A Preliminary Report,” *Lithos* 3, no. 1 (1970): 89–92.

53. H. O’Brien, E. Heilimo, and P. Heino, “The Archean Siilinjärvi Carbonatite Complex,” in *Mineral Deposits of Finland* (Elsevier, 2015), 327–343.

54. K. Puustinen, *Geology of the Siilinjärvi Carbonatite Complex, Eastern Finland*, ser. Bulletin (Geologian tutkimuskeskus (Finland)) (Geol. Tutkimuslaitos Otaniemi, 1971), no. Nr. 249.

55. T. Al-Ani, F. Molnár, P. Lintinen, and S. Leinonen, “Geology and Mineralogy of Rare Earth Elements Deposits and Occurrences in Finland,” *Minerals* 8, no. 8 (2018): 356.

56. R. Jackisch, S. Lorenz, M. Kirsch, R. Zimmermann, L. Tusa, M. Pirttijärvi, A. Saartenoja, H. Ugalde, Y. Madriz, M. Savolainen, and R. Gloaguen, “Integrated Geological and Geophysical Mapping of a Carbonatite-Hosting Outcrop in Siilinjärvi, Finland, Using Unmanned Aerial Systems,” *Remote Sensing* 12, no. 18 (2020): 2998.

57. S. Decrée, M. Savolainen, J. Mercadier, V. Debaille, S. Höhn, H. Frimmel, and J.-M. Baele, “Geochemical and Spectroscopic Investigation of Apatite in the Siilinjärvi Carbonatite Complex: Keys to Understanding Apatite Forming Processes and Assessing Potential for Rare Earth Elements,” *Applied Geochemistry* 123 (2020): 104778.

58. T. Al Ani and O. Sarapää, “Geochemistry and Mineral Phases of REE in Jammi Carbonatite Veins and Fenites, Southern End of the Sokli Complex, NE Finland,” *Geochemistry: Exploration, Environment, Analysis* 13, no. 3 (2013): 217–224.

59. F. Wall, V. N. Niku-Paavola, C. Storey, A. Müller, and T. Jeffries, “Xenotime-(Y) from Carbonatite Dykes at Lofdal, Namibia: Unusually Low LREE:HREE Ratio in Carbonatite, and the First Dating of Xenotime Overgrowths on Zircon,” *The Canadian Mineralogist* 46, no. 4 (August 2008): 861–877.

60. A. Williams-Jones, R. Wollenberg, S. Bodeving, G. Simandl, and M. Neetz, “Hydrothermal Fractionation of the Rare Earth Elements and the Genesis of the Lofdal REE Deposit, Namibia,” in *Symposium on Strategic and Critical Materials Proceedings, November 13–14* (2015): 125–130.